Chapter 2
Electron Paramagnetic Resonance Theory

2.1 Historical Review

In 1921, Gerlach and Stern observed that a beam of silver atoms splits into two lines when it is subjected to a magnetic field [1–3]. While the line splitting in optical spectra, first found by Zeeman in 1896 [4, 5], could be explained by the angular momentum of the electrons, the *s*-electron of silver could not be subject to such a momentum, not to mention that an azimuthal quantum number $l = 1/2$ cannot be explained by classical physics. At that time, quantum mechanics was still an emerging field in physics and it took another three years until this anormal Zeeman effect was correctly interpreted by the joint research of Uhlenbeck, a classical physicist, and Goudsmit, a fellow of Paul Ehrenfest [6, 7]. They postulated a so-called 'spin', a quantized angular momentum, as an intrinsic property of the electron. This research marks the cornerstone of electron paramagnetic resonance (EPR) spectroscopy which is based on the transitions between quantized states of the resulting magnetic moment.

Cynically, the worst event in the twentieth century boosted the development of EPR spectroscopy as after World War II suitable microwave instrumentation was readily available from existing radar equipment. This lead to the observation of the first EPR spectrum by the Russian physicist Zavoisky in 1944 [8, 9] already one year before the first nuclear magnetic resonance (NMR) spectrum was recorded [10, 11]. The development of EPR and NMR went in the same pace during the first decade though NMR was by far more widely used. But in 1965, NMR spectroscopy experienced its final boost with the development of the much faster Fourier transform (FT) NMR technique which also opened the development of completely new methodologies in this field [12]. The corresponding pulse EPR spectroscopy suffered from expensive instrumentation, the lack of microwave components, sufficiently fast digital electronics and intrinsic problems of limited microwave power. Although the first pulse EPR experiment was reported by Blume already in 1958 [13], pulse EPR was conducted by only a small number of research groups over several decades.

M. J. N. Junk, *Assessing the Functional Structure of Molecular Transporters by EPR Spectroscopy*, Springer Theses, DOI: 10.1007/978-3-642-25135-1_2,

In the 1980s, the required equipment became cheaper and manageable and the first commercial pulse EPR spectrometer was released to the market [14], followed only ten years later by the first commercial high field spectrometer [15]. This development of equipment promoted the invention of new and the advancement of already existing methods. Nowadays, a vast EPR playground is accessible to an ever growing research community, which became as versatile as the spectroscopic technique itself.

2.2 EPR Fundamentals

2.2.1 Preface

While NMR is a standard spectroscopic technique for the structural determination of molecules, the closely related EPR spectroscopy is still sparsely known by many scientists. This discrepancy originates from the lack of naturally occurring paramagnetic systems due to the fact that the formation of a chemical bond is inherently coupled to the pairing of electrons and a resulting overall electron spin of $S = 0$.

This lack of EPR-active materials is both the biggest disadvantage and the biggest advantage of the method. On the one hand, the method is restricted to few existing paramagnetic systems, radicals and transition metal complexes with a residual electron spin. On the other hand, this selectivity turns out advantageous in the study of complex materials, since only few paramagnetic species lead to interpretable EPR spectra.

Since most materials are diamagnetic, paramagnetic species have to be artificially introduced as tracer molecules. Dependent on the manner of introduction, they are called spin labels or spin probes [16]. While spin labels are covalently attached to the system of interest, no chemical linkage is formed between spin probes and the material (see Sect. 2.6.1). In both cases, the tracer molecules are sensitive to their local surrounding in terms of structure and dynamics and thus allow an indirect *molecular* observation of the materials' properties [17, 18].

Additionally, dipole–dipole couplings between two electrons allow for distance measurements in the highly relevant range of 1.5–8 nm [19–21]. Attached to selected sites in biological and synthetic macromolecules, structural information of such complex materials becomes accessible [22–25]. This approach turns out especially powerful if the systems under investigation lack long-range order and scattering methods cannot be applied for structural analysis. Magnetic resonance techniques as intrinsically local methods do not require this constraint and EPR as one of only few methods allows for the structural characterization of these amorphous nanoscopic samples with a high selectivity and sensitivity [26–28].

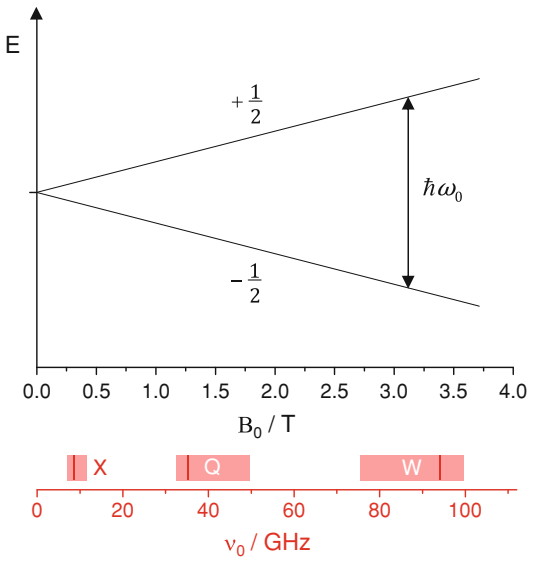

Fig. 2.1 Splitting of the energy levels of an electron spin subjected to a magnetic field with corresponding resonance frequencies, $g = g_e$, and typical EPR microwave bandsf

2.2.2 Resonance Phenomenon

Analogous to the orbital angular momentum **L**, the spin angular momentum **S** gives rise to a magnetic momentum **μ**

$$\boldsymbol{\mu} = \mathrm{h}\gamma_e \mathbf{S} = -g\beta_e \mathbf{S} \tag{2.1}$$

with the magnetogyric ratio of the electron γ_e, the Bohr magneton $\beta_e = e\hbar/2m_e$, and the g-factor $g \approx 2$. The exact g-value for a free electron of $g_e = 2.0023193043617(15)$ is predicted by quantum electrodynamics and is the most accurately determined fundamental constant by both theory and experiment [29]. If the electron is subjected to an external magnetic field $\mathbf{B}_0^{\mathrm{T}} = (0, 0, \mathrm{B}_0)$,[1] the energy levels of the degenerate spin states split depending on their magnetic quantum number $m_S = \pm 1/2$ and the strength of the magnetic field B_0,

$$E = \pm\frac{1}{2} g\beta_e B_0. \tag{2.2}$$

Irradiation at a frequency ω_0, which matches the energetic difference ΔE between the two states, results in absorption,

$$\Delta E = \hbar\omega_0 = g\beta_e B_0. \tag{2.3}$$

[1] The correct term for **B** is magnetic induction. The term magnetic field originates from older magnetic resonance literature and is still commonly used while its symbol **H** was replaced by **B**.

The spectroscopic detection of this absorption is the fundamental principle of EPR spectroscopy. The resonance frequency $\omega_0 = -\gamma_e B_0$ is named Larmor frequency after J. Larmor, who described the analogous motion of a spinning magnet in a magnetic field in 1904. A schematic of the resonance phenomenon is depicted in Fig. 2.1.

For $g = 2$, magnetic fields between 0.1 and 1.5 Tesla, easily achievable with electro-magnets, result in resonance frequencies in the microwave (mw) regime between 2.8 and 42 GHz. Historically, mw frequencies are divided into bands. Most commercially available spectrometers operate at X-band ($\sim$9.5 GHz), Q-band ($\sim$36 GHz), or W-band ($\sim$95 GHz). All EPR measurements in this work were performed at X-band.

2.2.3 Magnetization

In general, EPR spectroscopy is conducted on a large ensemble of spins. The actual quantity detected is the net magnetic moment per unit volume, the macroscopic magnetization **M** (Eq. 2.7). The relative populations of the two energy states $|\alpha\rangle$ $(m_S = +1/2)$ and $|\beta\rangle$ $(m_S = -1/2)$ are given by the Boltzmann distribution

$$\frac{n_\alpha}{n_\beta} = \exp\left(-\frac{\Delta E}{kT}\right). \tag{2.4}$$

The excess polarization is described by the polarization P

$$P = \frac{n_\alpha - n_\beta}{n_\alpha + n_\beta} = \frac{1 - \exp(-\Delta E/kT)}{1 + \exp(-\Delta E/kT)}. \tag{2.5}$$

In a high temperature approximation $(\Delta E \ll kT)$, which is valid for all experiments described in this thesis, the polarization is given by

$$P = \tanh\left(\frac{\hbar\gamma_e B_0}{2kT}\right) \approx \frac{\hbar\gamma_e B_0}{2kT}. \tag{2.6}$$

For a static magnetic field in z-direction, as described above, the equilibrium magnetization yields

$$\mathbf{M}_0 = \frac{1}{V}\sum_i \mu_i = \frac{1}{2} N\hbar\gamma_e P\mathbf{e}_z, \tag{2.7}$$

where $N = n_\alpha + n_\beta$ is the total number of spins. It is proportional to the magnetic field and inversely proportional to the temperature. Since the polarization is proportional to the magnetogyric ratio of the electron, the magnetization is proportional to γ_e^2, explaining the high sensitivity of EPR in comparison to NMR. Later in this thesis, the polarization difference between electrons and protons is utilized to enhance the magnitude of NMR signals (Chap. 6).

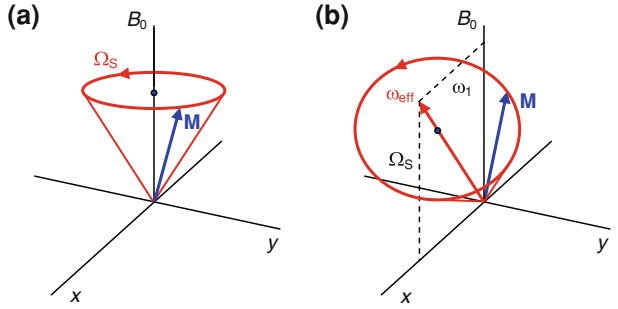

Fig. 2.2 **a** Free precession of the magnetization vector **M** in the rotation frame with the precession frequency $\Omega_S = \omega_0 - \omega_{mw}$. **b** Nutation of the magnetization vector during off-resonant mw irradiation with a circularly polarized mw field along x with amplitude ω_1. Reproduced from [76] by permission of Oxford University Press (www.uop.com)

2.2.4 Bloch Equations

Following the Larmor theorem, the motion of a magnetic moment in a magnetic field gives rise to a torque. For a single spin, this torque is given by

$$\hbar \frac{d\mathbf{S}}{dt} = \boldsymbol{\mu} \times \mathbf{B}. \tag{2.8}$$

Using the net magnetization **M** and dividing by V, we get

$$\hbar \frac{d\mathbf{M}}{dt} = \mathbf{M} \times \gamma_e \mathbf{B}. \tag{2.9}$$

When the magnetization is in equilibrium and a static magnetic field is applied along z, the magnetization vector is time-invariant and cannot be detected. However, any displacement from the z-axis results in a precessing motion around this axis with the Larmor frequency Ω_0, giving rise to a detectable alternating magnetic field. It is convenient to define a coordinate system that rotates counterclockwise with the microwave frequency Ω_{mw}. In this coordinate system, the magnetization vector rotates with a precession frequency $\Omega_S = \Omega_0 - \Omega_{mw}$ (Fig. 2.2a), which is the resonance offset between the Larmor and the mw frequency.

To detect an EPR signal, besides $\mathbf{B}_0$ an additional oscillating mw field $\mathbf{B}_1^T = (B_1 \cos(\omega_{mw} t), B_1 \sin(\omega_{mw} t), 0)$ is applied along x, which moves the magnetization vector away from its equilibrium position (Fig. 2.2b). For on-resonant mw irradiation ($\Omega_S = 0$), the effective nutation frequency ω_{eff} equals $\omega_1 = g\beta_e B_1/\hbar$ and the magnetization vector precesses around the x-axis while the magnetization vector is hardly affected if the mw frequency is far off-resonant ($\Omega_S \gg \omega_1$).

To fully describe the motion of the magnetization vector, relaxation effects also need to be considered. The longitudinal relaxation time T_1 characterizes the

process(es) that make the magnetization vector return to its thermal equilibrium state while the transverse relaxation time T_2 describes the loss of coherence in the transverse plane due to spin–spin interactions. Felix Bloch first derived the famous equation of motion which fully describes the evolution of the magnetization [30]

$$\hbar \frac{d\mathbf{M}}{dt} = \mathbf{M}(t) \times \gamma_e \mathbf{B}(t) - \mathbf{R}(\mathbf{M}(t) - \mathbf{M}_0) = \begin{pmatrix} -\Omega_S M_y - M_x/T_2 \\ \Omega_S M_x - \omega_1 M_z - M_y/T_2 \\ \omega_1 M_y - (M_z - M_0)/T_1 \end{pmatrix}. \tag{2.10}$$

The magnetic field $\mathbf{B}$ consists of the static magnetic field $\mathbf{B}_0$ as well as the oscillating mw field $\mathbf{B}_1$,

$$\mathbf{B} = \begin{pmatrix} B_1 \cos(\omega_{mw} t) \\ B_1 \sin(\omega_{mw} t) \\ B_0 \end{pmatrix}, \tag{2.11}$$

and the relaxation tensor is given by

$$\mathbf{R} = \begin{pmatrix} T_2^{-1} & 0 & 0 \\ 0 & T_2^{-1} & 0 \\ 0 & 0 & T_1^{-1} \end{pmatrix}. \tag{2.12}$$

2.2.5 Continuous Microwave Irradiation

The most facile EPR experiment can be realized by continuous microwave irradiation of a sample placed in a magnetic field and detection of the microwave absorption. It is extremely difficult to produce a microwave source that provides a variable frequency range of several octaves with a sufficient amplitude and frequency stability. Hence, the microwave frequency (the quantum) is kept constant, while the magnetic field (the energy level separation) is varied.

A second EPR characteristic is determined by the instrumentation. The detector, a microwave diode, is sensitive to a broad frequency range. To reduce the frequency range of the detected noise, the EPR signal is modulated by a sinusoidal modulation of the magnetic field and only the modulated part of the diode output voltage is detected. Besides a drastically enhanced signal-to-noise ratio (SNR), this method implies the detection of the first derivative of the absorption spectrum rather than the absorption line itself. Although the detected signal is proportional to the modulation amplitude $\Delta B_0, \Delta B_0$ should not exceed one-third of the line width ΔB_{PP} (cf. Fig. 2.3) to avoid disturbed line shapes.

After a sufficiently long continuous microwave irradiation, the magnetization will reach a stationary state and the time derivatives of the magnetization vector vanish. In this case, the Bloch equation (Eq. 2.10) becomes a linear system of equations and the components of the magnetic field vector are given by

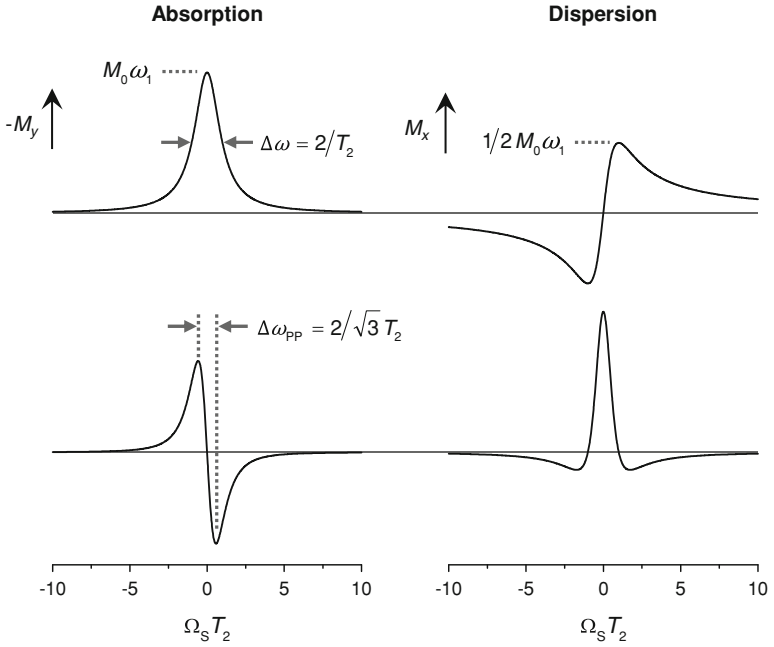

Fig. 2.3 *Top*: Lorentzian absorption and dispersion lineshapes calculated by Eqs. 2.15 and 2.16. *Bottom*: first derivative of the Lorentzian lines as observed in CW EPR spectroscopy

$$M_x = M_0\omega_1 \frac{\Omega_S T_2^2}{1 + \Omega_S^2 T_2^2 + \omega_1^2 T_1 T_2}, \tag{2.13a}$$

$$M_y = -M_0\omega_1 \frac{T_2}{1 + \Omega_S^2 T_2^2 + \omega_1^2 T_1 T_2}, \tag{2.13b}$$

$$M_z = M_0 \frac{1 + \Omega_S^2 T_2^2}{1 + \Omega_S^2 T_2^2 + \omega_1^2 T_1 T_2}. \tag{2.13c}$$

M_Z is called longitudinal magnetization and cannot be detected with conventional experimental setups. The components M_x and M_y are called transverse magnetization or coherence and can be measured simultaneously in a quadrature-detection scheme with two microwave reference signals phase shifted by 90° with respect to each other. In this case, a complex signal

$$V = -M_y + iM_x \tag{2.14}$$

is obtained.

For low microwave powers, i.e. $\omega_1^2 T_1 T_2 \ll 1$, the last term of the denominator in Eqs. 2.11–2.13 vanishes. In this *linear regime*, M_x and M_y are proportional to ω_1. The real part of the complex signal amounts to

$$-M_y = M_0\omega_1 \frac{T_2}{1+\Omega_S^2 T_2^2} = M_0\omega_1 \frac{T_2^{-1}}{T_2^{-2}+\Omega_S^2}. \tag{2.15}$$

This corresponds to a Lorentzian absorption line with a width T_2^{-1} and an amplitude $M_0\omega_1$. The imaginary part is given by

$$M_x = M_0\omega_1 \frac{\Omega_S T_2^2}{1+\Omega_S^2 T_2^2} = M_0\omega_1 \frac{\Omega_S}{T_2^{-2}+\Omega_S^2}, \tag{2.16}$$

corresponding to a Lorentzian dispersion line. Both line shape functions as well as their first derivatives are illustrated in Fig. 2.3. Since the dispersion line suffers from broad flanks and decreased amplitudes, only absorption lines are recorded, which offer a better SNR and a better resolution in presence of multiple lines.

In the analysis of first derivative spectra, the definition of a peak-to-peak line width Γ_{PP} is favorable. It is related to the full width at half maximum (FWHM) of the respective absorption line by

$$\frac{\Gamma_{PP}}{\Gamma_{FWHM}} = 3^{-1/2}. \tag{2.17}$$

On an angular frequency scale, the peak-to-peak line width is given by $\Delta\omega_{PP} = 2/\sqrt{3}T_2$. In magnetic field swept spectra, the relation

$$\Delta B_{PP} = \frac{2}{\sqrt{3}T_2}\frac{\hbar}{g\beta_e} \tag{2.18}$$

holds when the spectrum is not inhomogeneously broadened by unresolved hyperfine couplings. In the latter case, the spectrum consists of Gauss or Voigt lines rather than of pure Lorentzian signals.

EPR is a spectroscopic method relying on a purely quantum mechanical construct, the electron spin. So far, this has been described in the picture of classical physics. In the next section, we will proceed to a quantum-mechanical description, and to the spin Hamiltonian which describes all magnetic interactions of the spin with its environment.

2.3 Types of Interactions and Spin Hamiltonian

The spin Hamiltonian can be derived by the Hamiltonian of the whole system by separating the energetic contributions involving the spin from all other contributions [31]. It contains all interactions of the electron spin with the external magnetic field and internal magnetic moments i.e. other spins in the vicinity of the electron spin. Dependent on the number of interacting spins J, the spin Hamiltonian spans a Hilbert space with the dimension

$$n_H = \prod_k (2J_k + 1), \tag{2.19}$$

which describes the number of energy levels of the system. The energy of a paramagnetic species in the ground state with an effective electron spin S and n coupled nuclei with spins I is described by the static spin Hamiltonian

$$\mathcal{H}_0 = \mathcal{H}_{\mathrm{EZ}} + \mathcal{H}_{\mathrm{ZFS}} + \mathcal{H}_{\mathrm{HF}} + \mathcal{H}_{\mathrm{NZ}} + \mathcal{H}_{\mathrm{NQ}} + \mathcal{H}_{\mathrm{NN}}. \tag{2.20}$$

The terms describe the electron Zeeman interaction $\mathcal{H}_{\mathrm{EZ}}$, the zero-field splitting $\mathcal{H}_{\mathrm{ZFS}}$, hyperfine couplings between the electron spin and the nuclear spins $\mathcal{H}_{\mathrm{HF}}$, the nuclear Zeeman interactions $\mathcal{H}_{\mathrm{NZ}}$, the quadrupolar interactions $\mathcal{H}_{\mathrm{NQ}}$ for nuclear spins with $I > 1/2$, and spin–spin interactions between pairs of nuclear spins $\mathcal{H}_{\mathrm{NN}}$. The different terms of the spin Hamiltonian in Eq. 2.20 are ordered according to their typical energetic contribution. All energies will be given in angular frequency units.

2.3.1 Electron Zeeman Interaction

The interaction between the electron spin and the external magnetic field is described by the electron Zeeman term

$$\mathcal{H}_{\mathrm{EZ}} = \frac{\beta_{\mathrm{e}}}{\hbar} \mathbf{B}_0^{\mathrm{T}} \mathbf{g} \mathbf{S}, \tag{2.21}$$

which is the dominant term of the spin Hamiltonian for usually applied magnetic fields (high field approximation). Since both spin operator $\mathbf{S}$ and the external magnetic field $\mathbf{B}_0$ are explicitly orientation-dependent, $\mathbf{g}$ assumes the general form of a tensor with the components

$$\mathbf{g} = \begin{pmatrix} g_{xx} & g_{xy} & g_{xz} \\ g_{yx} & g_{yy} & g_{yz} \\ g_{zx} & g_{zy} & g_{zz} \end{pmatrix}. \tag{2.22}$$

It can be diagonalized via Euler angle transformation of the magnetic field vector into the molecular coordinate system of the radical to yield

$$\mathbf{g} = \begin{pmatrix} g_{xx} & 0 & 0 \\ 0 & g_{yy} & 0 \\ 0 & 0 & g_{zz} \end{pmatrix}. \tag{2.23}$$

The deviation of the $\mathbf{g}$ principal values from the g_{e} value of the free electron spin and its orientation dependence is caused by the spin–orbit coupling. Since the orbital angular momentum $\mathbf{L}$ is quenched for a non-degenerate ground state, only the interaction of excited states and ground state leads to an admixture of the orbital angular momentum to the spin angular momentum. The $\mathbf{g}$ tensor can be expressed by [32]

$$\mathbf{g} = g_{\mathrm{e}}\mathbf{1} + 2\lambda\mathbf{\Lambda} \tag{2.24}$$

with the spin–orbit coupling constant λ and the symmetric tensor $\mathbf{\Lambda}$ with elements

$$\Lambda_{ij} = \sum_{n \neq 0} \frac{\langle \psi_0 | L_i | \psi_n \rangle \langle \psi_n | L_j | \psi_0 \rangle}{\epsilon_0 - \epsilon_n}. \tag{2.25}$$

Each element Λ_{ij} describes the interactions of the SOMO ground state ψ_0 with energy ε_0 and the nth excited state ψ_n with energy ε_n. A large deviation from g_e results from a small energy difference between the SOMO and the lowest excited state and a large the spin–orbit coupling. For most organic radicals, the excited states are high in energy and $g_{jj} \approx g_e$. Larger deviations are observed for transition metal complexes, which also benefit from the fact that the spin–orbit coupling as a relativistic effect is proportional to the molecular mass of the atom.

In solution, the orientation dependence of the **g** tensor is averaged by fast molecular motion and an isotropic g-value is observed, which amounts to

$$g_{\text{iso}} = \frac{1}{3}\left(g_{xx} + g_{yy} + g_{zz}\right). \tag{2.26}$$

2.3.2 Nuclear Zeeman Interaction

Analogous to the electron Zeeman interaction, nuclear spins couple to the external magnetic field. This contribution is described by the nuclear Zeeman term

$$\mathcal{H}_{\text{NZ}} = -\frac{\beta_n}{\hbar} \sum_k g_{n,k} \mathbf{B}_0^{\text{T}} \mathbf{I}_k. \tag{2.27}$$

The spin quantum number I and the g_n factor are inherent properties of a nucleus. In most experiments, the nuclear Zeeman interaction can be considered isotropic. It hardly influences EPR spectra, however affects nuclear frequency spectra measured by EPR techniques (cf. Sect. 2.10).

2.3.3 Hyperfine Interaction

The hyperfine interaction is one of the most important sources of information in EPR spectroscopy. It characterizes interactions between the electron spin and nuclear spins in its vicinity. Hence, it provides information about the direct magnetic environment of the spin. Its contribution to the Hamiltonian is given by

$$\mathcal{H}_{\text{HF}} = \sum_k \mathbf{S}^{\text{T}} \mathbf{A}_k \mathbf{I}_k = \mathcal{H}_{\text{F}} + \mathcal{H}_{\text{DD}}. \tag{2.28}$$

$\mathbf{A}$ is the hyperfine coupling tensor and $\mathbf{I}_k$ the spin operator of the kth coupled nucleus. This Hamiltonian can be further subdivided in an isotropic part $\mathcal{H}_\mathrm{F}$ and a dipolar part $\mathcal{H}_\mathrm{DD}$.

The nuclear magnetic moment gives rise to a dipole–dipole interaction between electron and nuclear spin, which acts through space. In general, the interaction between two magnetic dipoles $\boldsymbol{\mu}_1$ and $\boldsymbol{\mu}_2$ is given by

$$E = \frac{\mu_0}{4\pi}\frac{1}{r^3}\left[\boldsymbol{\mu}_1^\mathrm{T}\boldsymbol{\mu}_2 - \frac{3}{r^2}\left(\boldsymbol{\mu}_1^\mathrm{T}\mathbf{r}\right)\left(\boldsymbol{\mu}_2^\mathrm{T}\mathbf{r}\right)\right]. \tag{2.29}$$

With the introduction of the dipolar coupling tensor $\mathbf{T}$, the dipolar term of the hyperfine interaction can be expressed by

$$\mathcal{H}_\mathrm{DD} = \sum_k \mathbf{S}^\mathrm{T}\mathbf{T}_k\mathbf{I}_k. \tag{2.30}$$

In the hyperfine principal axis system, $\mathbf{T}$ is approximately described by

$$\mathbf{T} = \frac{\mu_0}{4\pi}\frac{g_\mathrm{e}g_\mathrm{n}\beta_\mathrm{e}\beta_\mathrm{n}}{R^3}\begin{pmatrix}-1 & & \\ & -1 & \\ & & 2\end{pmatrix} = \begin{pmatrix}-T & & \\ & -T & \\ & & 2T\end{pmatrix}. \tag{2.31}$$

This representation neglects $\mathbf{g}$ anisotropies and spin–orbit couplings but is a good approximation as long as both effects are small. Since $\mathbf{T}$ is traceless, the dipolar part of the hyperfine interaction is averaged to zero by fast and isotropic rotation of the radical. In this case, only the isotropic part of the hyperfine interaction prevails. The energetic contributions of this so-called Fermi contact term

$$\mathcal{H}_\mathrm{F} = \sum_k a_{\mathrm{iso},k}\mathbf{S}^\mathrm{T}\mathbf{I}_k \tag{2.32}$$

are characterized by the isotropic hyperfine coupling constant

$$a_\mathrm{iso} = \frac{2}{3}\frac{\mu_0}{\hbar}g_\mathrm{e}g_\mathrm{n}\beta_\mathrm{e}\beta_\mathrm{n}|\psi_0(0)|^2. \tag{2.33}$$

This contribution originates, since an electron in a s-orbital possesses a finite electron spin density at the nucleus, $|\psi_0(0)|^2$. Via configuration interaction or spin polarization mechanisms, also electrons in orbitals with $l \neq 0$ contribute to the spin density at the nucleus and to the isotropic hyperfine coupling term [33].

2.3.4 Nuclear Quadrupole Interaction

Nuclei with $I \geq 1$ are characterized by a non-spherical charge distribution, which gives rise to a nuclear electrical quadrupole moment Q. This moment interacts with the electric field gradient at the nucleus, caused by electrons and nuclei in its

vicinity. With the traceless nuclear quadrupole tensor **P**, this contribution is described by

$$\mathcal{H}_{\mathrm{NQ}} = \sum_{I_k > 1/2} \mathbf{I}_k^{\mathrm{T}} \mathbf{P}_k \mathbf{I}_k. \tag{2.34}$$

In EPR spectra, nuclear quadrupole interactions cause resonance shifts and the appearance of forbidden transitions. These small second-order effects are difficult to observe. In nuclear frequency spectra recorded by EPR, quadrupole couplings manifest themselves as first-order splittings (cf. Sect. 4.3.2).

2.3.5 Nuclear Spin–Spin Interaction

The dipole–dipole interaction between two nuclear spins is given by

$$\mathcal{H}_{\mathrm{NQ}} = \sum_{I_k > 1/2} \mathbf{I}_i^{\mathrm{T}} \mathbf{d}^{(i,k)} \mathbf{I}_k. \tag{2.35}$$

The nuclear dipole coupling tensor $\mathbf{d}^{(i,k)}$ provides the main information source in solid-state NMR [26]. However, the coupling is far too weak to be observed in EPR spectra and usually it is not even resolved in nuclear frequency spectra.

2.3.6 Zero-Field Splitting

For spin systems with a group spin $S > 1/2$ and non-cubic symmetry, the dipole–dipole couplings between individual electron spins remove the energetic degeneracy of the ground state. This zero-field splitting causes an energy splitting even in the absence of an external magnetic field and is expressed by

$$\mathcal{H}_{\mathrm{ZFS}} = \mathbf{S}^{\mathrm{T}} \mathbf{D} \mathbf{S} \tag{2.36}$$

with the symmetric and traceless zero-field interaction tensor **D** and the group spin $\mathbf{S} = \sum_k \mathbf{S}_k$. In this thesis, only paramagnetic species with $S = 1/2$ are studied in detail. Thus, the zero-field splitting term of the spin Hamiltonian can be neglected.

2.3.7 Weak Coupling Between Electron Spins

Strongly interacting electron spins are characterized by a group spin, as discussed in the previous section. A system of two weakly coupled unpaired electrons is more conveniently described by two single spin Hamiltonians and additional terms, which arise from the coupling,

$$\mathcal{H}_0(S_1, S_2) = \mathcal{H}_0(S_1) + \mathcal{H}_0(S_2) + \mathcal{H}_{\text{exch}} + \mathcal{H}_{\text{dd}}. \tag{2.37}$$

These excess terms characterize the contributions due to spin exchange $\mathcal{H}_{\text{exch}}$ and dipole–dipole coupling $\mathcal{H}_{\text{dd}}$ [34].

2.3.7.1 Heisenberg Exchange Coupling

When two species approach each other close enough, the orbitals of the two spins overlap and the unpaired electrons can be exchanged. In solids, the upper limit of 1.5 nm can be exceeded in strongly delocalized systems [22]. In liquid solutions, the exchange interaction is mainly governed by the collision of paramagnetic species leading to strongly overlapping orbitals for short times.

Exchange coupling can be differentiated into an isotropic and anisotropic contribution and is characterized by the exchange coupling tensor $\mathbf{J}$. Its contribution to the static spin Hamiltonian is given by

$$\mathcal{H}_{\text{exch}} = \mathbf{S}_1^{\text{T}}\mathbf{J}\mathbf{S}_2 = J_{12}\mathbf{S}_1^{\text{T}}\mathbf{S}_2 \tag{2.38}$$

The last term of Eq. 2.38 only applies for organic radicals, since the anisotropic part of the exchange tensor $\mathbf{J}$ can be neglected. In a system $S_1 = S_2 = 1/2$, the isotropic part can be described in terms of chemical bonding. Ferromagnetically coupled spins form a weakly bonded triplet state with $S = 1$, while a weakly antibonded singulet state $(S = 0)$ is formed in case of antiferromagnetic coupling.

2.3.7.2 Dipole–Dipole Interaction

The dipole–dipole interaction between two electrons is treated in analogy to the dipolar coupling between an electron and a nucleus (Sect. 2.3.3). Since the measurement of dipolar couplings is a powerful tool to extract distance information and will be utilized extensively in the next section, we shall have a closer look on the inner working of the equations.

The interaction of two classic dipoles was already given in Eq. 2.29. Distributed randomly in space, as depicted in Fig. 2.4 (left), the interaction energy depends on their relative orientation to the connecting vector and can be calculated by

$$E = \frac{\mu_0}{4\pi}\frac{1}{r_{12}^3}(2\cos\theta_1\cos\theta_2 - \sin\theta_1\sin\theta_2\cos\chi). \tag{2.39}$$

In the high field approximation, the dipolar coupling to the external magnetic field dominates all other contributions. Hence, the dipoles align parallel to $\mathbf{B}_0$ (Fig. 2.4 right), and Eq. 2.39 simplifies to

$$E = \frac{\mu_0}{4\pi}\frac{1}{r_{12}^3}\left(1 - 3\cos^2\theta\right). \tag{2.40}$$

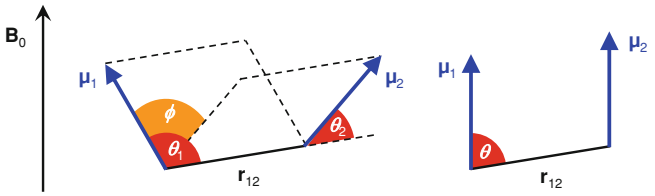

Fig. 2.4 Schematic representation of two interacting magnetic dipoles. *Left*: arbitrary orientation of the dipoles in space. The angles between the dipoles and the connection vector **r** are denoted θ_1 and θ_2. The angular offset between the two spanned planes is characterized by the dihedral angle χ. *Right*: orientation of both dipoles parallel to the external magnetic field $\mathbf{B}_0$. Adapted from [79] with permission from the author

In this approximation and neglecting **g** anisotropy, the spin Hamiltonian as a quantum-mechanical analogue amounts to

$$\mathcal{H}_{\mathrm{dd}} = \mathbf{S}^{\mathrm{T}}\mathbf{D}\mathbf{S} = \frac{\mu_0}{4\pi\hbar}\frac{1}{r_{12}^3} g_1 g_2 \beta_{\mathrm{e}}^2 \left[\mathbf{S}_1^{\mathrm{T}}\mathbf{S}_2 - \frac{3}{r_{12}^2}\left(\mathbf{S}_1^{\mathrm{T}}\mathbf{r}_{12}\right)\left(\mathbf{S}_2^{\mathrm{T}}\mathbf{r}_{12}\right)\right]. \tag{2.41}$$

The dipolar coupling tensor **D** can be expressed in its principal axes frame as

$$\mathbf{D} = \frac{\mu_0}{4\pi\hbar}\frac{g_1 g_2 \beta_{\mathrm{e}}^2}{r_{12}^3}\begin{pmatrix} -1 & & \\ & -1 & \\ & & 2 \end{pmatrix} = \begin{pmatrix} -\omega_{\mathrm{DD}} & & \\ & -\omega_{\mathrm{DD}} & \\ & & 2\omega_{\mathrm{DD}} \end{pmatrix}. \tag{2.42}$$

Since the frequency is proportional to r_{12}^{-3}, the distance between the coupled spin pair can be retrieved. This is discussed in detail in Sect. 2.11, where the corresponding pulse EPR method is introduced.

2.4 Anisotropy in EPR Spectra

Many interactions in magnetic resonance are anisotropic or have anisotropic components. In disordered samples, i.e. non-crystalline materials lacking long-range order, the radicals are distributed randomly with respect to the external magnetic field. If the rotational motion does not average the orientation of the paramagnetic species, these anisotropic interactions lead to powder spectra. For a given microwave frequency, spins fulfill the resonance condition at different magnetic field positions depending of their orientation. This leads to broadened spectra with characteristic line shapes.

2.4.1 g Anisotropy

As stated in Sect. 2.3, the Electron-Zeeman interaction depends on the absolute orientation of the molecule with respect to the external magnetic field.

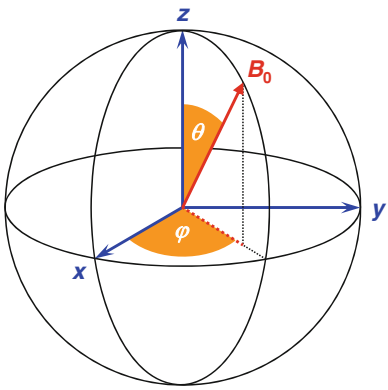

Fig. 2.5 Definition of the elevation angle θ and the azimuth φ in a unit sphere depicting the molecular coordinate system (collinear to the principal elements of the diagonalized **g** tensor, g_{xx}, g_{yy}, and g_{zz}) and the magnetic field vector $\mathbf{B}_0$

The orientation of the molecule can be characterized by the elevation angle θ and the azimuth φ of a spherical coordinate system. θ characterizes the angle between the molecular z-axis and the vector of the magnetic field $\mathbf{B}_0$. φ denotes the angle between its projection on the molecular xy-plane and the x-axis (Fig. 2.5).

Each point of the anisotropic spectrum is characterized by an effective g-value by the relation

$$B_0 = \frac{\hbar\omega_0}{g_{\text{eff}}\beta_e}. \tag{2.43}$$

In general, the effective g-value depends on both spherical angles and can be calculated by

$$g(\theta,\varphi) = (g_{xx}^2 \sin^2\theta\cos^2\varphi + g_{yy}^2 \sin^2\theta\sin^2\varphi + g_{zz}^2\cos^2\theta)^{1/2}. \tag{2.44}$$

In case of axial symmetry with $g_{zz} = g_\parallel$ aligned parallel to the unique axis of the molecular frame and $g_{xx} = g_{yy} = g_\perp$ aligned perpendicular to this axis, the **g** tensor is given by

$$\mathbf{g} = \begin{pmatrix} g_\perp & 0 & 0 \\ 0 & g_\perp & 0 \\ 0 & 0 & g_\parallel \end{pmatrix}. \tag{2.45}$$

Hence, the φ dependence vanishes and the effective g-value amounts to

$$g(\theta) = (g_\perp^2 \sin^2\theta + g_\parallel^2\cos^2\theta)^{1/2}. \tag{2.46}$$

Characteristic anisotropically broadened powder spectra for paramagnetic species with axial and orthorhombic symmetries are displayed in Fig. 2.6. Unit spheres illustrate the orientational contributions at the principal g-values. Since the intensity scales with the number of contributing orientations, the maximum spectral intensity is observed at effective g-values corresponding to $g_\perp$ and g_{yy}, respectively.

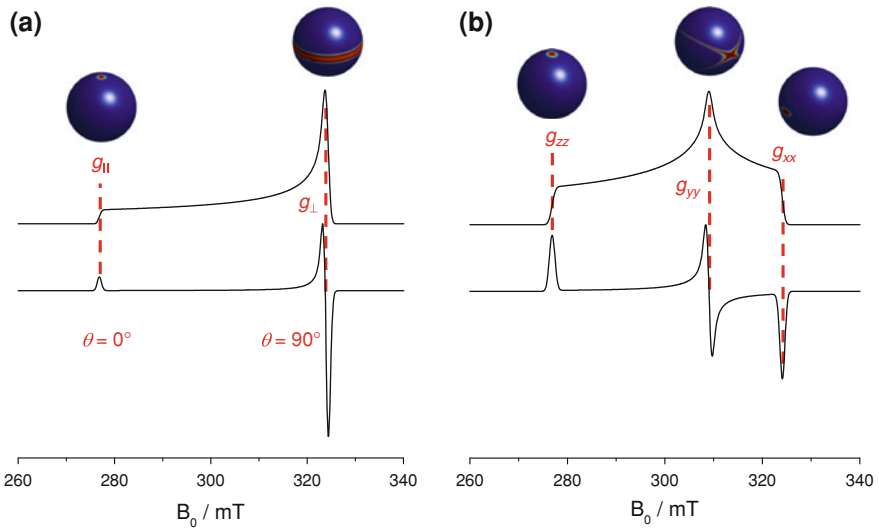

Fig. 2.6 Simulated absorption (*top*) and first derivative (*bottom*) powder spectra with anisotropic **g** tensors at a microwave frequency of 9.3 GHz. **a** Axial symmetry with $g_{\perp} = 2.05$ and $g_{||} = 2.4$. **b** Orthorhombic symmetry with $g_{xx} = 2.05$, $g_{yy} = 2.15$, and $g_{zz} = 2.4$. Red spots on the unit spheres mark orientations that contribute to the spectra at magnetic field positions corresponding to the principal g-values upon excitation by a 32 ns mw pulse. Adapted from [79] with permission from the author

2.4.2 Combined Anisotropies in Real Spectra

Besides the g-value, both the hyperfine coupling constant and the zero–field splitting constant have anisotropic components which influence the line shape in CW EPR spectra. The explicit orientation dependence of dipole–dipole interactions between different unpaired electrons and its consequence for the DEER experiment is treated in Sects. 2.11 and 3.4.

In this thesis, no paramagnetic species with an effective electron spin $S > 1/2$ is studied which would give rise to zero-field splitting. However, the hyperfine anisotropy plays an important role for many radicals. It is given by the magnitude of the dipole–dipole interaction between the electron and the nuclear spin.

Simulated powder spectra of a Jahn–Teller distorted copper(II) complex and a nitroxide are shown in Fig. 2.7, which exhibit both **g** and **A** anisotropy. The **g** tensor of the copper complex is axially symmetric due to four identical equatorial ligands, while the nitroxide shows unique orientational dependences along all molecular axes. The hyperfine anisotropy, however, is approximately axially symmetric in both cases. In either case, the principal axes of the **g** and the **A** tensor coincide. A simplified explanation for the observed hyperfine anisotropy can be given as follows: The majority of the electron density is distributed in molecular orbitals aligned parallel to the molecular z-axis of the paramagnetic

moiety (see also Sect. 2.6.2). Thus, the dipolar coupling with the proximate nuclei (^{63}Cu with $I = 3/2$ and ^{14}N with $I = 1$, respectively) in this direction dominates and gives rise to the highest hyperfine coupling, $A_{\parallel}$ or A_{zz}. The significantly lower hyperfine coupling values along the x- and the y-direction are not fully resolved.

The superposition of two spectral anisotropies accounts for the decreased orientational selectivity in comparison to the purely **g** anisotropic spectra displayed in Fig. 2.6.

2.5 Dynamic Exchange

In this section, we will take a closer look on how the spectral parameters are affected when a paramagnetic species undergoes a transition on the EPR timescale ($\sim$ns) that changes its electronic structure. This transition can be either a chemical reaction or any process that changes the conformation of the radical or its environment (see Sect. 2.6.4). In all cases, the resonance frequency of the EPR transition is affected due to a change of the hyperfine coupling, or the **g** tensor, or both. Additionally, the line width is affected by the average time frame during which this process happens.

This process will be referred to as *dynamic exchange* throughout this thesis since it is the dynamic transition of a spin probe between two different environments that is responsible for the spectral effects observed in Chap. 7. In magnetic resonance textbooks, the process is commonly called *chemical exchange* and treated analogously.

If we consider a transition from a species A to a species B with the rate constants forward and backward, k_1 and k_{-1},

$$\mathrm{A} \underset{k_{-1}}{\overset{k_{-1}}{\rightleftharpoons}} \mathrm{B}, \tag{2.47}$$

the average lifetimes of both species are given by

$$\tau_\mathrm{A} = \frac{1}{k_1} \quad \text{and} \quad \tau_\mathrm{B} = \frac{1}{k_{-1}}. \tag{2.48}$$

At equilibrium, the rates for the transition back and forward must be equal, so that the fractions ρ_j of each site are related to the average lifetimes by

$$\frac{\rho_\mathrm{A}}{\tau_\mathrm{A}} = \frac{\rho_\mathrm{B}}{\tau_\mathrm{B}}. \tag{2.49}$$

For a two-site problem, the equilibrium constant amounts to

$$K = \frac{\tau_\mathrm{B}}{\tau_\mathrm{A}} = \frac{\rho_\mathrm{B}}{\rho_\mathrm{A}} \tag{2.50}$$

and the fractions ρ_j can be expressed in terms of the average lifetimes by

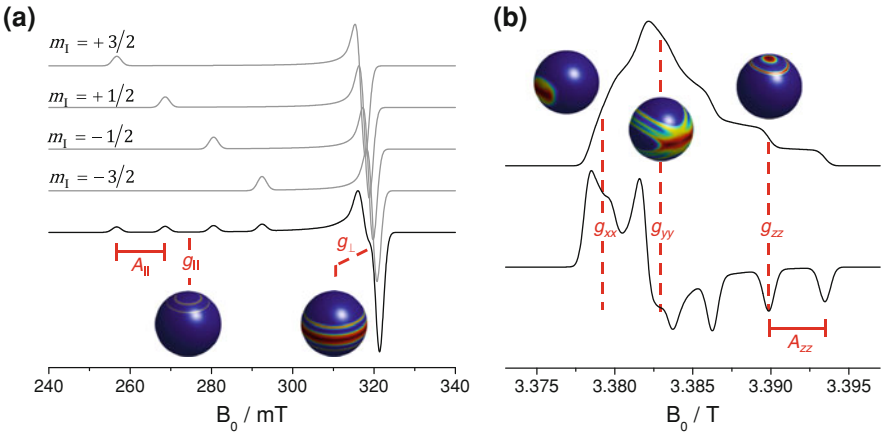

Fig. 2.7 Simulated EPR spectra for paramagnetic species with several anisotropic contributions. **a** Copper(II) spectrum with axial symmetric and collinear **g** and **A** tensors ($g_\perp = 2.085$, $g_\parallel = 2.42$ and $A_\perp = 28.0$ MHz, $A_\parallel = 403.6$ MHz) at a microwave frequency of 9.3 GHz. A 100% isotopic abundance of ^{63}Cu is assumed. Hypothetical spectra corresponding to different quantum numbers of the copper nucleus are displayed in gray. **b** W-band (95 MHz) absorption (*top*) and first derivative (*bottom*) EPR spectrum of a nitroxide radical with an orthorhombic **g** tensor ($g_{xx} = 2.0087$, $g_{yy} = 2.0065$, and $g_{zz} = 2.0023$) and a collinear hyperfine coupling tensor $A_{xx} = A_{yy} = 18.2$ MHz and $A_{zz} = (100.9$ MHz). Excited orientations are illustrated in red on unit spheres at principal g-value field positions. Note the decreased orientational selectivity in comparison to Fig. 2.6 due to the additional hyperfine contribution

$$\rho_A = \frac{\tau_A}{\tau_A + \tau_B} \quad \text{and} \quad \rho_B = \frac{\tau_B}{\tau_A + \tau_B}. \tag{2.51}$$

As stated in Sect. 2.2.5, the detected EPR signal V consists of a real and an imaginary part, $V = -M_y + iM_x$. Extending the Bloch equations, one can write

$$\frac{dV}{dt} = -\frac{dM_y}{dt} + i\frac{dM_x}{dt} = -V\left[\frac{1}{T_2} + i\Omega_S\right] + \omega_1 M_0. \tag{2.52}$$

In the present case, each species j gives rise to an EPR transition with a resonance frequency $\omega + \omega_j$. The contributions to the total magnetization from each site can be expressed as

$$\frac{dV_j}{dt} = -V\left[\frac{1}{T_{2,j}} + i(\Omega_S + \omega_j)\right] + \omega_1 M_{0,j}. \tag{2.53}$$

One can further write $M_{0,j} = \rho_j M_0$ and $W_j = \Omega_S + \omega_j$. Using the short notation $T_j = T_{2,j}$ and adding the appropriate terms for the transfer of spins between the two sides, Eqs. 2.54, 2.55 are obtained [35].

$$\frac{dV_A}{dt} = -V\left[\frac{1}{T_A} + i(\Omega_S + \omega_A)\right] + \rho_A \omega_1 M_0 + \frac{V_B}{\tau_B} - \frac{V_A}{\tau_A} \tag{2.54}$$

$$\frac{dV_B}{dt} = -V\left[\frac{1}{T_B} + i(\Omega_S + \omega_B)\right] + \rho_B\omega_1 M_0 + \frac{V_A}{\tau_A} - \frac{V_B}{\tau_B} \tag{2.55}$$

In equilibrium, the time derivatives can be set to zero. The real part of the magnetization is given by

$$-M_y = -M_{y,A} - M_{y,B}. \tag{2.56}$$

For the two-site problem under consideration, one yields the analytical expression

$$-M_y = \omega_1 M_0 \frac{\begin{array}{c}\left\{\tau_A + \tau_B + \tau_A\tau_B(\rho_A T_B^{-1} + \rho_B T_A^{-1})\right\}\left\{\begin{array}{c}\tau_A\tau_B(T_A^{-1}T_B^{-1} - W_A W_B)\\ +\tau_A T_A^{-1} + \tau_B T_B^{-1}\end{array}\right\}\\ +\tau_A\tau_B(\rho_A W_B + \rho_B W_A)\left\{\tau_A W_A(1+\tau_B T_B^{-1}) + \tau_B W_B(1+\tau_A T_A^{-1})\right\}\end{array}}{\begin{array}{c}\left\{\tau_A\tau_B(T_A^{-1}T_B^{-1} - W_A W_B) + \tau_A T_A^{-1} + \tau_B T_B^{-1}\right\}^2\\ +\left\{\tau_A W_A(1+\tau_B T_B^{-1}) + \tau_B W_B(1+\tau_A T_A^{-1})\right\}^2\end{array}}. \tag{2.57}$$

A simplification of Eq. 2.57 can be achieved by applying limiting conditions. In the limit of slow exchange, i.e. $\tau_j^{-1} \ll \Delta\omega = |\omega_A - \omega_B|$, the signal consists of two Lorentzian lines, centered at ω_A and ω_B, with line widths T_A^{-1} and T_B^{-1} and relative intensities ρ_A and ρ_B, respectively,

$$-M_y = \omega_1 M_0\left[\rho_A\frac{T_A^{-1}}{T_A^{-2} + W_A^2} + \rho_B\frac{T_B^{-1}}{T_B^{-2} + W_B^2}\right]. \tag{2.58}$$

As the lifetime decreases, but still in the slow exchange regime, each line receives an additional contribution to its line width $T_{exch}^{-1} = \tau_j^{-1}$. Upon further decrease of the lifetime, the two lines merge to a single broadened Lorentzian line at the weighted frequency $\rho_A\omega_A + \rho_B\omega_B$, when $\tau_j^{-1} > \Delta\omega$.

In this condition of fast exchange, the result assumes the simplified form

$$-M_y = \omega_1 M_0\frac{\rho_A T_A^{-1} + \rho_B T_B^{-1} + \rho_A^2\rho_B^2(\Delta\omega)^2(\tau_A + \tau_B)}{\left[\rho_A T_A^{-1} + \rho_B T_B^{-1} + \rho_A^2\rho_B^2(\Delta\omega)^2(\tau_A + \tau_B)\right]^2 + (\rho_A W_A + \rho_B W_B)^2}. \tag{2.59}$$

Defining a reduced lifetime τ by

$$2\tau^{-1} = \tau_A^{-1} + \tau_B^{-1} \tag{2.60}$$

and using Eq. 2.51, the exchange contribution in the condition of fast exchange amounts to

$$T_{exch}^{-1} = \frac{1}{2}\rho_A\rho_B(\Delta\omega)^2\tau. \tag{2.61}$$

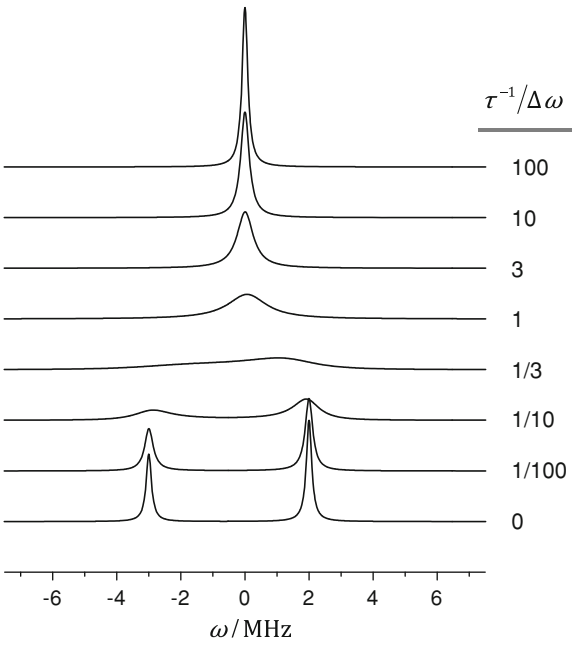

Fig. 2.8 Calculated absorption spectra of a two-spin system with resonance frequencies $\omega_A = 2$ MHz and $\omega_B = -3$ MHz, Lorentzian line widths $T_j^{-1} = 0.1$ MHz, and the relative lifetimes $\tau_A/\tau_B = 3/2$ under evolution of dynamic exchange. As the reduced lifetime τ approaches the frequency difference $\Delta\omega$, the two lines centered at ω_A and ω_B broaden and merge to a single broadened line, which sharpens again at still shorter lifetimes τ

At still shorter lifetimes, the line width becomes independent of the exchange rate and the spectrum consists of a single sharp Lorentzian line with a weighted resonance frequency and line width. The evolution of an EPR spectrum under dynamic exchange is visualized in Fig. 2.8.

2.6 Nitroxides as Spin Probes

As mentioned in Sect. 2.2.1, one major drawback of EPR spectroscopy is related to the small number of paramagnetic systems. The structural determination of these systems by EPR can nonetheless be achieved by introduction of paramagnetic tracer molecules, so-called spin probes or spin labels. Nitroxides, stable free radicals with the structural unit R_2NO, mark the by far most important class of these paramagnetic molecules. The chemical structures of common nitroxide derivatives are shown in Fig. 2.9. In this thesis, nitroxides with structural motives **1** and **4** are used.

The stability of nitroxides can be explained by the delocalized spin density ($\sim$40% on the nitrogen atom, $\sim$60% on the oxygen atom) and full methyl substitution in β-position. The latter provides sterical hindrance as well as removal of the structural motif of a β-proton. Thus, typical radical reactions like dimerizations and disproportionations are inhibited.

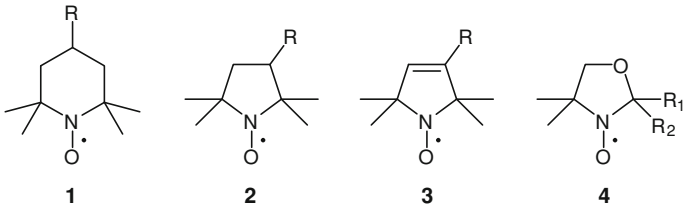

Fig. 2.9 Chemical structures of common nitroxide spin probes. Depicted are derivatives of **a** 2,2,6,6-tetramethylpiperidine-1-oxyl (TEMPO), **b** 2,2,5,5-tetramethylpyrrolidine-1-oxyl (PROXYL), **c** 2,2,5,5-tetramethylpyrroline-1-oxyl (dehydro-PROXYL), and **d** 4,4-dimethyl-oxazolidine-1-oxyl (DOXYL)

2.6.1 Spin Probe versus Spin Label

Spin labels are chemically attached to the material of interest while spin probes interact non-covalently with the system. The method of introduction depends on the system itself and on the type of requested information.

Spin probes are favorable for studies of macromolecules and supramolecular assemblies, as their structure and dynamics are mostly governed by non-covalent interactions. Via self-assembly, the spin probes selectively choose the environment that offers the most attractive interactions. They can also be seen as tracers for small guest molecules like drugs or analytes and deliver information about the host–guest relationship.

The introduction of spin labels is more demanding as the structural unit bearing the unpaired electron needs to be chemically attached to a functional group of the system. This method implies a bigger modification of the system, which could alter its function. It can still be worth the effort and risk, as the electron spin is locally restricted to a specific site of the system and distance measurements can be applied to gain structural information of its three-dimensional structure.

In the last few years, this so-called site directed spin labeling in combination with distance measurements has become a widely used tool for the structural determination of proteins and other (biological) macromolecules [23, 36–38].

2.6.2 Quantum Mechanical Description

For equally distributed nitroxides in dilute solution ($c < 2$ mM), many terms of the static spin Hamiltonian (Eq. 2.20) are irrelevant. In this case, the interactions of the unpaired electron and the magnetic ^{14}N nucleus ($I = 1$) are sufficiently characterized by the electron and nuclear Zeeman interactions and by the hyperfine coupling term, yielding a spin Hamiltonian

$$\mathcal{H}_{\mathrm{NO}} = \beta_{\mathrm{e}} \mathbf{B}_0^{\mathrm{T}} \mathbf{g} \mathbf{S} - \frac{\beta_{\mathrm{N}} g_{\mathrm{N}}}{\hbar} \mathbf{B}_0^{\mathrm{T}} \mathbf{I} + \mathbf{S}^{\mathrm{T}} \mathbf{A} \mathbf{I}. \tag{2.62}$$

The quadrupolar contribution of the ^{14}N nucleus is neglected in this description. The energy eigenvalues are determined through solution of the Schrödinger equation. For a fast, isotropic rotation, six eigenstates with energies

$$E_{NO} = g_{iso}\beta_e B_0 m_S - g_N\beta_N B_0 m_I + a_{iso} m_S m_I \tag{2.63}$$

are obtained. This equation also holds for anisotropic motion, if g_{iso} and a_{iso} are substituted by the effective values in the respective orientation. The corresponding energy level diagram is depicted in Fig. 2.10. Three allowed EPR transitions with frequencies ω_I are determined by the selection rules $\Delta m_S = \pm 1$ and $\Delta m_I = 0$,

$$\Delta E_{NO} = \hbar\omega_I = g_{iso}\beta_e B_0 + a_{iso} m_I. \tag{2.64}$$

Although the nuclear Zeeman interaction does not affect the EPR transition frequencies, the nuclear frequencies, detectable by advanced EPR methods, depend on the interplay of nuclear Zeeman interaction and hyperfine coupling. A detailed description is given in Sect. 2.10, when the corresponding method is introduced.

The molecular coordinate system of nitroxides is presented in Fig. 2.11. The $2p_z$ orbital of the nitrogen atom defines the z-axis. The x-axis is directed along the N–O bond and the y-axis is directed perpendicular to the xz-plane. If spectra were recorded that only detected orientations along the principal axes, they would assume the form illustrated in Fig. 2.11. The center line position marks the principal **g** tensor element, and the spacing is determined by the corresponding principal element of the hyperfine tensor. The maximum hyperfine coupling value is found along z, since most spin density resides in the π^* orbital along this axis.

2.6.3 Nitroxide Dynamics

The motion of the spin probe is strongly influenced by the dynamics and local structure of its surrounding. Thus, the analysis of nitroxide dynamics delivers indirect information about the system of interest. EPR is sensitive to rotational diffusion rather than translational motion, since only angular motions relative to the external magnetic field affect the magnetic interactions and the spectral line shapes. If the spin probe rotates very fast, the hyperfine couplings in different directions average to an isotropic value a_{iso} and a spectrum is obtained that consists of three equal lines. On the other hand, an anisotropic powder spectrum is obtained when rotational motion is prohibited (cf. Sect. 2.4).

Between these two extremes, the spectral shape strongly depends on the time frame of the rotational diffusion. For isotropic Brownian rotational motion, it is characterized by the rotational correlation time τ_c. Formally, τ_c is calculated by summation of all autocorrelation functions of the Wigner rotation matrices $\mathbf{D}(\Omega(t))$,

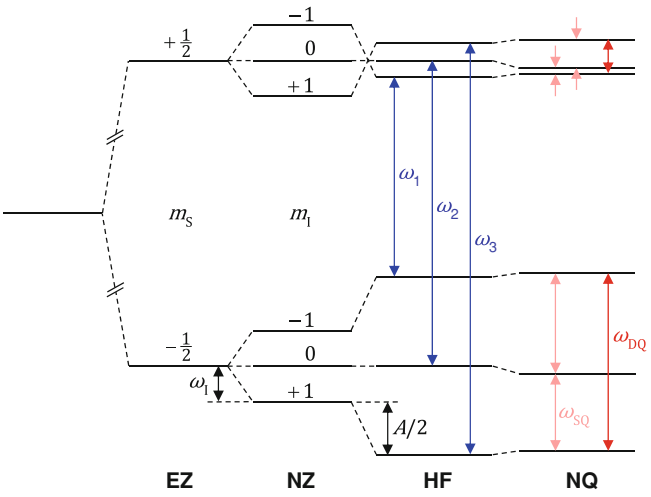

Fig. 2.10 Energy level diagram for an $S = 1/2,\ I = 1/2$ spin system in the strong coupling case $|A/2| > |\Omega_I|$ with allowed EPR transitions (*blue*) and nuclear single quantum (SQ) and double quantum (DQ) transitions (*red*). The nuclear quadrupole contribution is included

$$\tau_c = \int_{t_0}^{\infty} \langle D^l_{m,n}(\Omega(t)) | D^l_{m,n}(\Omega(t_0)) \rangle dt. \tag{2.65}$$

A detailed derivation is given in the literature [40, 41]. The rotational correlation time is related to the rotational diffusion coefficient by

$$\tau_c = \frac{1}{6D_R}. \tag{2.66}$$

The effect of the rotational diffusion on EPR spectra is shown in Fig. 2.12. In the regime of fast rotation (left hand side), the relative widths and heights of the spectral lines change due to increasing anisotropic contributions. The high-field line is most strongly affected since it experiences the cumulative effect of **g** and **A** anisotropy. The strongest spectral changes are observed at $\tau_c \sim 3$ ns, when the inverse rotational correlation time matches the contribution due to anisotropic line broadening. When the rotational motion is further restricted (slow motion regime), the separation of the outer extrema is a meaningful parameter to describe the spin probe dynamics [42].

Though there are established methods to infer the rotational correlation time in the fast motion regime from the relative heights of the central and high-field line [43, 44], these methods break down if the spectra consist of several overlapping species. Due to this fact, all rotational correlation times in this thesis were obtained by fitting of spectral simulations (cf. Sect. 2.7).

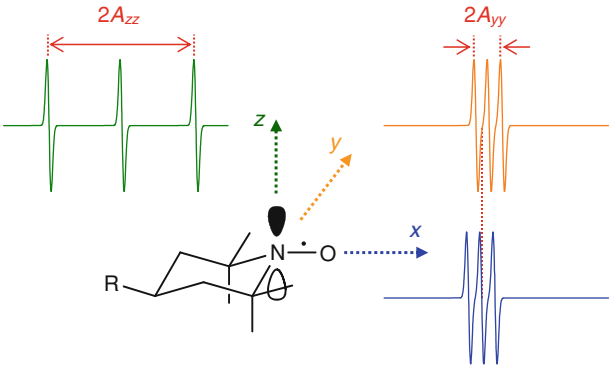

Fig. 2.11 Definition of the molecular coordinate system of nitroxides and hypothetical spectra for orientations along the principal axes. Collinear **g** and **A** tensors with principal values $g_{xx} = 2.0087$, $g_{yy} = 2.0065$, $g_{zz} = 2.0023$ and $A_{xx} = A_{yy} = 18.2$ MHz, $A_{zz} = 100.9$ MHz were assumed. Adapted from [39] with permission from the author

If the rotation of the nitroxide is hindered in several directions (e.g. due to chemical attachment), an anisotropy has to be introduced to the Brownian motion. In case of a fast rotation about one axis and a slower rotation about directions perpendicular to that axis, the rotational diffusion coefficient can be expressed in its principal axes frame by [40, 45]

$$\mathbf{D}_\mathrm{R} = \begin{pmatrix} D_\perp & & \\ & D_\perp & \\ & & D_\parallel \end{pmatrix}. \tag{2.67}$$

Examples for more sophisticated approaches to account for spin probe dynamics are the macroscopic order microscopic disorder (MOMD) model and the slowly relaxing local structure (SRLS) model [46, 47]. They are not introduced in detail, since in this work it was sufficient to analyze the spin probe rotation in terms of isotropic and anisotropic rotational motion.

2.6.4 Environmental Influences

In addition to dynamics, spin probes also provide information about their local environment. The electronic structure of a nitroxide is slightly altered depending on the interactions with molecules in its surrounding. In solvents of different polarity and proticity (pH), the same spin probe thus shows slightly different hyperfine coupling constants and g-values. For X-band spectra, this effect is illustrated in Fig. 2.13. The alterations of the spectra are small but add up at the high-field line. Thus, spin probes in different nanoscopic environments in inhomogeneous samples can be distinguished and analyzed separately. This constitutes

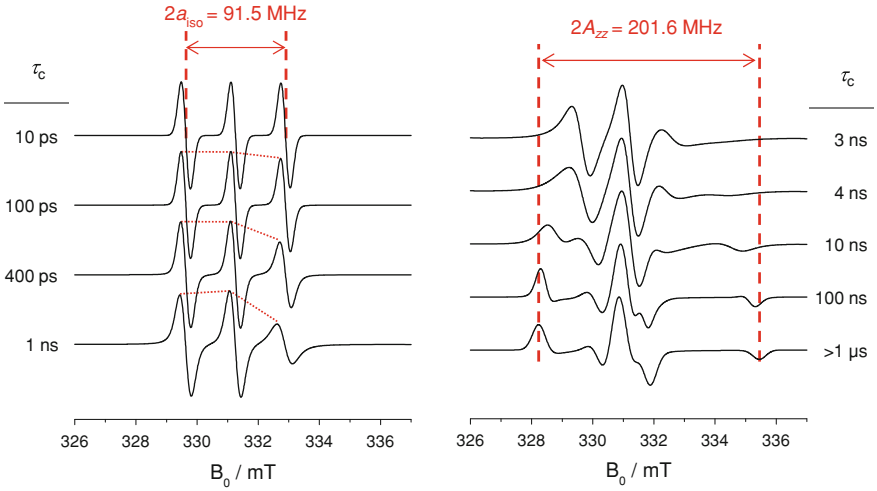

Fig. 2.12 EPR spectral dependence on rotational dynamics for isotropic rotational diffusion in the regimes of fast motion (*left*) and slow tumbling (*right*). The spectra were obtained by simulations with routines accounting for fast motion $\tau_c = (10–400\ \text{ps})$, intermediate/slow motion $\tau_c = (1–100\text{ns})$, and powder type spectra in the rigid limit ($\tau_c > 1\mu\text{s}$) (cf. Sect. 2.7). The principal values of **g** and **A** are listed in Fig. 2.11. Adapted from [79] with permission from the author

the main source of information for the characterization of thermoresponsive systems in Chaps. 5 and 7.

In polar solvents, the zwitterionic resonance structure in Fig. 2.14b is stabilized and spin density is transferred to the nitrogen nucleus. This leads to an increase of A_{zz} and to a decrease of g_{xx} since the deviation of g_{xx} from g_e mainly depends on the spin–orbit coupling in the oxygen orbitals.

At a given polarity, the SOMO–LUMO energy difference increases, if the oxygen atom acts as hydrogen acceptor (Fig. 2.14a). Hence, the spin–orbit contribution decreases, and the deviation of g_{xx} from g_e becomes less significant (cf. Sect. 2.3.1). In high-field spectra, the correlation of g_{xx} and A_{zz} can be utilized to distinguish between polar and protic solvents [48, 49]. At X-band and for fast rotating spin probes, the above-mentioned effects manifest themselves in changes of a_{iso} and g_{iso}.

2.7 CW Spectral Analysis via Simulations

Only for simple CW EPR spectra, all structural and dynamic parameters can be inferred by a straightforward analysis. This method breaks down in case of overlapping spectral components, complex rotational dynamics, and unresolved couplings. Here, much information is buried in the line shape and cannot be retrieved in a non-trivial manner. In this case, the reproduction of the spectrum by

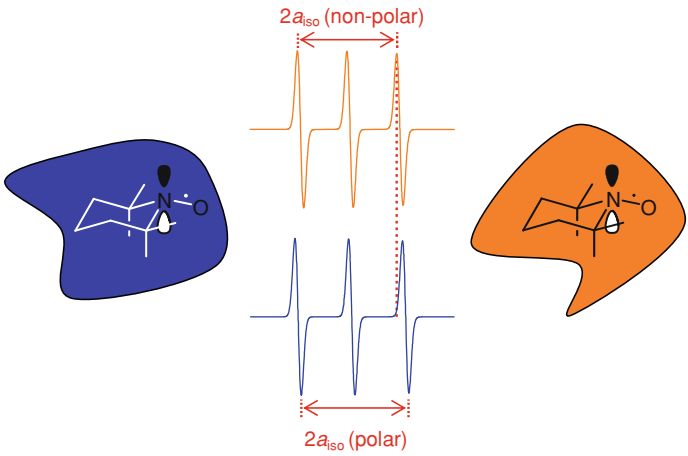

Fig. 2.13 Schematic depiction of spin probes in hydrophilic (*blue*) and hydrophobic (*orange*) environments and corresponding fast-motion spectra with g_{iso} (polar) = 2.0060, a_{iso} (polar) = 48.2 MHz and g_{iso} (non-polar) = 2.0063, a_{iso} (non-polar) = 44.3 MHz

a quantum-mechanical simulation is the method of choice. The spectral parameters of interest can then be read out from the simulation.

Most CW EPR spectra in this thesis were analyzed by spectral simulations, performed with home-written Matlab programs based on various EasySpin routines. EasySpin is a simulation software developed by Stoll and Schweiger that provides routines for spectral simulations in a wide range of dynamic conditions [50, 51]. It subdivides four regimes of rotational motion: the isotropic limit, fast motion, slow motion, and the rigid limit.

The fast tumbling of radicals in the isotropic limit leads to a complete averaging of rotational motion and the spectrum consists of symmetric lines with equal widths. Corresponding spectra are computed by a diagonalization of the isotropic spin Hamiltonian. The resulting energy levels are obtained by the Breit-Rabi formulae [52].

In the fast motion regime (e.g. Fig. 2.12 left), small anisotropy effects change the heights and widths of the EPR transitions depending on their nuclear quantum number m_I. Applying the Redfield theory, these effects are treated as small perturbation [53, 54].

In slow motion (e.g. Fig. 2.12 right), the perturbation approach does not sufficiently account for the large spectral influence of rotational motion. Spectra are calculated by solving the stochastic Liouville equation in an approach developed by Schneider and Freed [45]. The rotational motion is accounted for by the diffusion superoperator, which depends on the model and the orientational distribution of rotation.

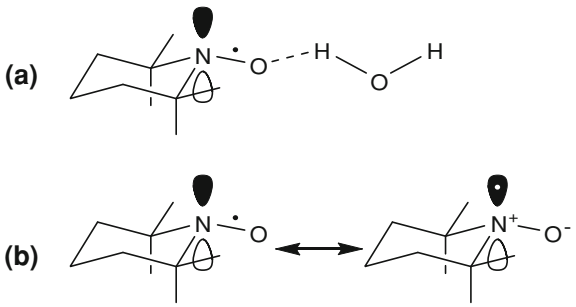

Fig. 2.14 Origin of the polarity and proticity dependence of nitroxide spectra. **a** Hydrogen bonding leads to a decrease of the spin–orbit coupling. **b** A stabilization of the zwitterionic resonance structure causes an increase of the spin density at the nitrogen atom. The combined effects lead to a decrease of g_{iso} and to an increase of a_{iso}

In the rigid limit, the orientations of the paramagnetic molecules are static. In this case, the positions, intensities and widths of all resonance lines are computed for each orientation by modeling the energy level diagram [55].

2.8 Time Evolution of Spin Ensembles

Although a CW EPR spectrum is influenced by all magnetic interactions of the spin Hamiltonian, only few dominating interactions are sufficiently resolved for an accurate analysis. The different contributions to the spin Hamiltonian can be separated by pulse EPR spectroscopy. Thus, small interactions of the electron spin with remote electron and nuclear spins can be resolved and precisely measured. Since in pulse EPR spectroscopy, microwave irradiation is not applied continuously but in defined time intervals, the time evolution of the spins has to be considered explicitly.

In this section, a formalism is introduced that describes the quantum-mechanical state of spin ensembles. Further, it is shown how this formalism can be applied to EPR. Based on this foundation, those pulse methods applied in this thesis are introduced in the following sections.

2.8.1 The Density Matrix

The quantum-mechanical expectation value of an observable O in a (single) spin system described by the wave function ψ is given by

$$\langle O \rangle = \langle \psi | O | \psi \rangle. \tag{2.68}$$

In this representation, the explicit form of the wave function has to be known. The wave function can be developed in a set of orthogonal eigenfunctions k

$$|\psi(t)\rangle = \sum_k c_k(t)|k\rangle, \tag{2.69}$$

yielding a new expression for the expectation value

$$\langle O\rangle = \sum_{k,l} \overline{c_k c_l^*}\langle l|O|k\rangle. \tag{2.70}$$

In reality, a spin ensemble is detected rather than a single spin. Their properties are best described by the Hermitian density operator

$$\boldsymbol{\rho} = |\psi\rangle\langle\psi| = \sum_{k,l} \overline{c_k c_l^*}|k\rangle\langle l| \tag{2.71}$$

with the matrix elements

$$\rho_{kl} = \overline{c_k c_l^*} = \langle k|\boldsymbol{\rho}|l\rangle. \tag{2.72}$$

The off-diagonal matrix element ρ_{kl} quantifies coherences between states $|k\rangle$ and $|l\rangle$, while the diagonal elements ρ_{kk} represent the population of the state $|k\rangle$. Ensemble averaging is done by an averaging of the coefficients c_k, c_l. The expectation value of an observable in an ensemble is then given by

$$\langle\overline{O}\rangle = \mathrm{Tr}(\boldsymbol{\rho}\mathbf{O}), \tag{2.73}$$

which is conveniently independent of the wave function. In analogy to the time dependent Schrödinger equation

$$\frac{d|\psi\rangle}{dt} = -i\mathcal{H}|\psi(t)\rangle, \tag{2.74}$$

the evolution of the density matrix under the spin Hamiltonian is given by the Liouville–von Neumann equation

$$\frac{d|\boldsymbol{\rho}\rangle}{dt} = -i[\mathcal{H}|\boldsymbol{\rho}]. \tag{2.75}$$

The Liouville–von Neumann equation neglects relaxation which can be introduced by the relaxation super-operator Ξ to yield

$$\frac{d|\boldsymbol{\rho}\rangle}{dt} = -i[\mathcal{H}|\boldsymbol{\rho}] - \Xi\big[\boldsymbol{\rho}(t) - \boldsymbol{\rho}_{\mathrm{eq}}\big]. \tag{2.76}$$

where $\boldsymbol{\rho}_{\mathrm{eq}}$ is the density operator of a spin system in thermal equilibrium. Since Ξ is time-independent, relaxation and time evolution of the spin ensemble can be treated separately.

The Liouville–von Neumann equation is readily solved when the Hamiltonian is constant for some time. The solution is most easily written in terms of operator exponentials

$$\boldsymbol{\rho}(t) = \exp(-i\mathcal{H}t)\boldsymbol{\rho}(0)\exp(-i\mathcal{H}t) = \mathbf{U}\boldsymbol{\rho}(0)\mathbf{U}^{\dagger}. \tag{2.77}$$

The propagator operator $\mathbf{U}$ and its Hermitian adjunct $\mathbf{U}^{\dagger}$ propagate the density operator in time via unitary transformations.

Solving the Liouville–von Neumann equation is more difficult when the Hamiltonian varies with time, e.g. in an experiment with pulsed microwave irradiation. In this case, it is convenient to divide the experiment in time intervals, during which the Hamiltonian is constant. In the framework of this so-called density operator formalism, propagators are consecutively applied for each time interval

$$\boldsymbol{\rho}(t_n) = \mathbf{U}_n \cdots \mathbf{U}_2\mathbf{U}_1\boldsymbol{\rho}(0)\mathbf{U}_1^{\dagger}\mathbf{U}_2^{\dagger} \cdots \mathbf{U}_n^{\dagger}. \tag{2.78}$$

2.8.2 Product Operator Formalism

For large spin systems, it is more convenient to decompose ρ into a linear combination of orthogonal basis operators B_j

$$\boldsymbol{\rho}(t) = \sum_j b_j(t)\mathbf{B}_j. \tag{2.79}$$

This product operator formalism is advantageous since each of the basis operators has a certain physical meaning [56]. Each set of basis operators consists of as many operators as there are elements in the density matrix. They span a basis with dimension $n_{\mathrm{H}}^2 = n_{\mathrm{L}}$, called Liouville space. For a single electron spin with $S = 1/2$, a Cartesian basis of $\mathbf{S}_x$, $\mathbf{S}_y$, $\mathbf{S}_z$ and half the identity operator $\frac{1}{2}\mathbf{1}$ can be used.

Not only density operators, but also Hamiltonians can be expressed in terms of Cartesian product operators. Thus, the evolution of the spin system can be described in the framework of product operators. In analogy to Eq. 2.77, the evolution of any operator A under another operator B can be expressed by

$$\begin{aligned} \exp(-i\phi B)A\exp(i\phi B) &= C \\ &\equiv A \xrightarrow{\phi B} C \end{aligned} \tag{2.80}$$

It is convenient to use the shorthand notation introduced in the lower part of eq. 2.80 to describe real EPR experiments. A generalized solution for $J = 1/2$ spin systems is given by [57]

$$\begin{aligned} A \xrightarrow{\phi B} A\cos\phi - i[B,A]\sin\phi \quad \forall\,[B,A] \neq 0, \\ A \xrightarrow{\phi B} A \quad \forall\,[B,A] = 0. \end{aligned} \tag{2.81}$$

If the Hamiltonian consists of a sum of product operator terms, they can be applied consecutively as long as they commute with each other.

2.8.3 Application to EPR

Before manipulating a spin system by microwave irradiation, its initial state must be known. The equilibrium state is characterized by a Boltzmann distribution (see also Eq. 2.4), i.e. the equilibrium density operator $\boldsymbol{\rho}_{\mathrm{eq}}$ is given by

$$\boldsymbol{\rho}_{\mathrm{eq}} = \frac{\exp(-\mathcal{H}_0\hbar/kT)}{\mathrm{Tr}[\exp(-\mathcal{H}_0\hbar/kT)]}. \tag{2.82}$$

In the high-field approximation, the dominating interaction is given by the electron Zeeman term and $\mathcal{H}_0 \cong \omega_{\mathrm{S}}\mathbf{S}_z$. Using the high-temperature approximation $\omega_{\mathrm{S}}\mathbf{S}_z \gg kT$ and performing a series expansion of the exponential, $\boldsymbol{\rho}_{\mathrm{eq}}$ can be approximated by

$$\boldsymbol{\rho}_{\mathrm{eq}} \cong \mathbf{1} - \frac{\hbar\omega_{\mathrm{S}}}{kT}\mathbf{S}_z. \tag{2.83}$$

The identity operator $\mathbf{1}$ is usually neglected as it is invariant throughout the experiment. Further, the constant factors are dropped and the equilibrium density operator is conveniently denoted as

$$\boldsymbol{\rho}_{\mathrm{eq}} = -\mathbf{S}_z. \tag{2.84}$$

The spin system leaves the state of thermal equilibrium by application of microwave pulses, i.e. (resonant) microwave irradiation during a time interval t_{P} in which the magnetization of the spin system is rotated by a flip angle

$$\beta = \omega_1 t_{\mathrm{P}}. \tag{2.85}$$

A pulse excites one or several transitions of a spin system depending on its excitation bandwidth, which is inversely proportional to t_{P}. A pulse is called non-selective, if it excites all allowed and partially allowed transitions on the spin system, or selective, if only one (or few) transitions are excited. Quantum-mechanically, a non-selective pulse applied from direction $i \in \{x, y, -x, -y\}$ is described by the product operator $\beta\mathbf{S}_i$. In this case, the static spin Hamiltonian during the pulse can be neglected and the pulse can be treated as an ideal, infinitely short pulse.

The spin Hamiltonian does, however, affect the further evolution of the spin system, as described in the Liouville–von Neumann equation (Eq. 2.77). The time of free evolution is thus characterized by the operator $\mathcal{H}_0 t$, or its linear combination of product operators.

In conclusion, starting from the point of thermal equilibrium, the fate of the spin system at the time of detection can be determined by consecutive application of product operators describing microwave pulses and free evolution.

2.8.4 The Vector Model

The vector model offers a somewhat more intuitive classical description for pulse EPR experiments, since the fate of the magnetization is followed in a pictorial view. The magnetization vector **M** was already introduced in Sect. 2.2.3 in the context of the Bloch equations (cf. Fig. 2.2). In analogy to the quantum-mechanical treatment, a pulse rotates **M** about the direction of the microwave field i by the flip angle β. In a shorthand notation, the pulse is referred to as β_i-pulse. Note that due to the sign convention of Eq. 2.1, the magnetization vector is aligned antiparallel to **S**.

The vector model is severely limited by the fact that it only applies to uncoupled spins, but it offers a conceptional insight in some key experiments. In the following chapters, it is used to illustrate the formation of spin echoes in addition to the quantum-mechanical treatment.

2.8.5 The ($S = 1/2$, $I = 1/2$) Model System

The principles of many pulse EPR experiments can be explained by considering a spin system consisting of one electron spin with $S = 1/2$ which is coupled to one nuclear spin with $I = 1/2$. The four-level scheme of such a system is depicted in Fig. 2.15a.

Since there is a certain probability for the nuclear spin to be flipped by a microwave pulse, also forbidden double and zero-quantum transitions are excited to some extent. Thus, both allowed and forbidden transitions with frequencies ω_{kl} give rise to an EPR spectrum illustrated in Fig. 2.15b.

The allowedness of a transition is characterized by $\eta = (\eta_\alpha - \eta_\beta)/2$. η_α and η_β define the directions of the nuclear quantization axes in the two m_S manifolds with respect to $\mathbf{B}_0$. Allowed transitions are weighted with $\cos\eta$, forbidden transitions with $\sin\eta$. The redistribution of coherences due to the excitation of forbidden transitions is called branching.

The two-spin system is fully described by the density matrix given in Fig. 2.15c. The diagonal elements ρ_{kk} represent populations of the corresponding

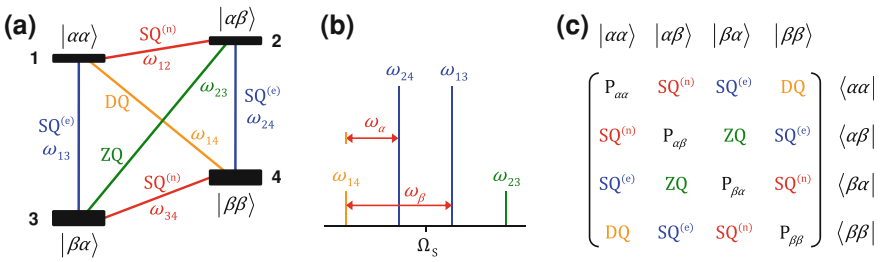

Fig. 2.15 Description of a weakly coupled $S = 1/2$, $I = 1/2$ spin system ($|\omega_I| > |A/2|$). **a** Energy level diagram with allowed single quantum (SQ) transitions of the electron (*blue*) and nucleus (*red*) and forbidden EPR double quantum (DQ) and zero quantum (ZQ) transitions (*orange*/*green*). **b** Corresponding stick spectrum. **c** Density matrix. The diagonal elements ρ_{kk} represent populations of the corresponding spin states, the off-diagonal elements ρ_{kl} represent coherences. Reproduced from [76] by permission of Oxford University Press (www.uop.com)

spin states, the off-diagonal elements ρ_{kl} represent coherences. The Cartesian basis of the two-spin system is obtained by multiplication of the Cartesian basis sets of the single spins.

$$\begin{aligned}\{\mathbf{A}_1, \mathbf{A}_2, \cdots, \mathbf{A}_{16}\} &= 2 \times \left\{\frac{1}{2}\mathbf{1}, \mathbf{S}_x, \mathbf{S}_y, \mathbf{S}_z\right\} \otimes \left\{\frac{1}{2}\mathbf{1}, \mathbf{I}_x, \mathbf{I}_y, \mathbf{I}_z\right\} \\ &= \left\{\begin{array}{c} \frac{1}{2}\mathbf{1}, \mathbf{S}_x, \mathbf{S}_y, \mathbf{S}_z, \mathbf{I}_x, \mathbf{I}_y, \mathbf{I}_z, 2\mathbf{S}_x\mathbf{I}_x, \\ 2\mathbf{S}_x\mathbf{I}_y, 2\mathbf{S}_x\mathbf{I}_z, 2\mathbf{S}_y\mathbf{I}_x, 2\mathbf{S}_y\mathbf{I}_y, 2\mathbf{S}_y\mathbf{I}_z, 2\mathbf{S}_z\mathbf{I}_x, 2\mathbf{S}_z\mathbf{I}_y, 2\mathbf{S}_z\mathbf{I}_z \end{array}\right\}\end{aligned} \tag{2.86}$$

The Hamiltonian of this spin system in its eigenbasis is given by

$$\mathcal{H}_0 = \Omega_S \mathbf{S}_z + \frac{\omega_+}{2}\mathbf{I}_z + \omega_- \mathbf{S}_z\mathbf{I}_z \tag{2.87}$$

with the nuclear combination frequencies

$$\begin{aligned}\omega_+ &= \omega_{12} + \omega_{34}, \\ \omega_- &= \omega_{12} - \omega_{34},\end{aligned} \tag{2.88}$$

as defined in Fig. 2.15b. Depending on the signs and magnitudes of the hyperfine coupling and nuclear Zeeman interaction, the nuclear frequencies ω_{12} and ω_{34} can assume positive or negative values. In some cases, it is convenient to use absolute values, defined by $\omega_\alpha = |\omega_{12}|$ and $\omega_\beta = |\omega_{34}|$.

2.9 Pulse EPR Methods Based on the Primary Echo

The standard experiment in NMR spectroscopy consists of a single $\pi/2$ pulse, which excites the whole spin system. Then, the free induction decay of the generated nuclear coherences is detected and the time-domain signal is Fourier transformed. The corresponding FT EPR technique is rarely used as it suffers from major problems. First, the excitation bandwidth of the shortest available microwave pulses ($t_{\pi/2} \approx 4$ ns) does not allow for a complete excitation of spin systems with even moderately broad spectral widths. More severely, the strong excitation pulse causes a ringing of the resonator, which prevents the recording of a signal for a certain time after the pulse. This so-called deadtime is $\sim$100 ns at X-band.

To circumvent the deadtime problem, most EPR experiments are based on the detection of electron spin echoes (ESE). The spin echo, invented by Hahn in 1950 [58], describes the reappearance of magnetization as an echo of the initial magnetization. The simplest representative of a spin echo, the primary echo (or Hahn echo), is observed after the pulse sequence $\pi/2 - \tau - \pi - \tau$, as illustrated in Fig. 2.16.

A vectorial explanation for the formation of the echo is given in Fig. 2.16 (bottom). The first $(\pi/2)_x$-pulse rotates the magnetization vector in the $-y$-direction. During the time of free evolution τ, spin packets with different Larmor frequencies gain a phase shift due to their different angular precession. In the rotating frame, the spin packets thus fan out according to their resonance offset Ω_S and the magnitude of the magnetization vector is decreased. The second $(\pi)_x$-pulse inverts the sign of the y-component. After the same evolution time τ, the phases of the different spin packets are refocused and the magnetization vector is maximized.

The same result is obtained in the framework of the product operator formalism (Eq. 2.81). Using the commutation rules for angular momentum operators

$$\begin{aligned} [\mathbf{S}_x, \mathbf{S}_y] &= i\mathbf{S}_z \\ [\mathbf{S}_y, \mathbf{S}_z] &= i\mathbf{S}_x \\ [\mathbf{S}_z, \mathbf{S}_x] &= i\mathbf{S}_y, \end{aligned} \tag{2.89}$$

the density operators for a system of isolated electron spins with $\mathcal{H}_0 = \Omega_s \mathbf{S}_z$ during a pulse sequence $(\pi/2)_x - \tau - \pi_x - t$ are given by

$$\begin{aligned} \boldsymbol{\rho}_{eq} = -\mathbf{S}_z \xrightarrow{\pi/2\mathbf{S}_x} \boldsymbol{\rho}_1 = \mathbf{S}_y \xrightarrow{\tau\Omega_s\mathbf{S}_z} \boldsymbol{\rho}_2(\tau) = \cos(\Omega_s\tau)\mathbf{S}_y - \sin(\Omega_s\tau)\mathbf{S}_x \\ \boldsymbol{\rho}_2(\tau) \xrightarrow{\pi\mathbf{S}_x} \boldsymbol{\rho}_3(\tau) = -\cos(\Omega_s\tau)\mathbf{S}_y - \sin(\Omega_s\tau)\mathbf{S}_x \\ \boldsymbol{\rho}_3(\tau) \xrightarrow{t\Omega_s\mathbf{S}_z} \boldsymbol{\rho}_4(\tau + t) = -\cos(\Omega_s(t-\tau))\mathbf{S}_y - \sin(\Omega_s(t-\tau))\mathbf{S}_x. \end{aligned} \tag{2.90}$$

For $\tau = t$, the arguments of the sin and cos functions vanish and the density operator $\boldsymbol{\rho}_4$ becomes

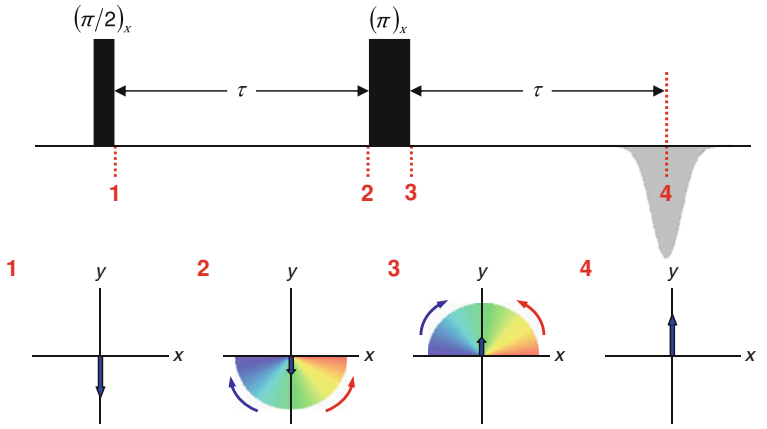

Fig. 2.16 *Top*: Formation of the primary echo after the pulse sequence $(\pi/2)_x - \tau - (\pi)_x - \tau$. *Bottom*: Graphical illustration of the magnetization vector at characteristic positions in the pulse sequence. Adapted from [79] with permission from the author

$$\boldsymbol{\rho}_4(2\tau) = -\mathbf{S}_y = -\boldsymbol{\rho}_1, \tag{2.91}$$

i.e. the (negative) spin state after the first pulse is retained.

The pulse sequence only refocuses inhomogeneous spin packets. Magnetization that is lost due to relaxation cannot be regained. This gives rise to an exponential decay of the echo as a function of τ. The characteristic time of the exponential decay, the phase memory time T_m, is closely related to the transverse relaxation time T_2.

2.9.1 ESE Detected Spectra

Though the pulse detection circumvents the deadtime problem, it does not overcome the insufficient excitation bandwidth. This problem can be solved by a sweep of the magnetic field analogous to the CW EPR technique. The microwave frequency and the pulse sequence are kept constant and the echo intensity is recorded as a function of the magnetic field. With this method, EPR absorption spectra are obtained.

At ambient temperature, echoes from paramagnetic species are usually not detectable due to short phase memory times which cause a complete relaxation of the signal by the time of detection. In this thesis, ESE-detected spectra were recorded at temperatures that provide for sufficiently long T_m times. Nitroxide spectra were usually recorded at 50 K, samples containing Cu^{2+} were measured at 10–20 K.

2.9.2 2-Pulse Electron Spin Echo Envelope Modulation (ESEEM)

In 1965, Rowan et al. [59] found that the spin echo decay of certain samples is modulated by nuclear frequencies and their combinations. This so-called electron spin envelope modulation (ESEEM) originates from the fact that the second $(\pi)_x$-pulse does not only invert the phase of the electron coherence but also redistributes this coherence among all allowed and forbidden electron spin transitions (cf. Sect. 2.8.5), which precess at different frequencies ω_{kl} [60].

After the time 2τ, only magnetization from the initially inverted electron coherence gives rise to an echo. The redistributed magnetization has acquired a phase ϕ and forms coherence transfer echoes that oscillate with $\cos(\phi)$. For the two-spin system, the phase is given by $\phi = (\omega_{kl} - \omega_{13})\tau$. The oscillations thus depend on the frequencies of the nuclear transitions ω_{12} and ω_{34} and the difference frequency ω_-.

The spin density operator at the time of echo formation can be calculated by substituting the spin Hamiltonian in Eq. 2.90 by that of Eq. 2.87. Thus, the modulation of the electron spin echo is described by

$$V_{2p}(\tau) = -S_y = 1 - \frac{k}{4}\left[2 - 2\cos(\omega_\alpha\tau) - 2\cos(\omega_\beta\tau) + \cos(\omega_+\tau) + \cos(\omega_-\tau)\right] \tag{2.92}$$

with a modulation depth parameter

$$k = \sin^2(2\eta) = \frac{9}{4}\left(\frac{\mu_0 g\beta_e}{4\pi B_0}\right)^2 \frac{\sin^2(2\theta)}{R^6}. \tag{2.93}$$

The last term of Eq. 2.93 is valid for weak hyperfine couplings and an isotropic g-value. In this case, the modulation depth is inversely proportional to the sixth power of the distance between the electron and the nuclear spin R [61].

Modulations of the electron spin echo due to couplings with j nuclei are multiplicative. Further, the modulations are superimposed by the exponential decay of the spin echo. Thus, the experimental time trace amounts to

$$V'_{2p}(\tau) = \exp\left(\frac{-2\tau}{T_m}\right)\prod_j V_{2p,j}(\tau). \tag{2.94}$$

To analyze the modulation frequencies, the exponential background is divided out and the time domain data is Fourier transformed into the frequency domain. The apparent resolution of the frequency domain spectrum is improved by zero filling, truncation artefacts are avoided by apodization. These methods apply to the frequency analysis of all ESEEM techniques.

2.10 Pulse EPR Methods Based on the Stimulated Echo

Schemes based on the stimulated echo are among the most commonly applied techniques in pulse EPR spectroscopy. The pulse sequence of a stimulated echo can be viewed as a modified primary echo sequence, in which the second π-pulse is divided in two $\pi/2$-pulses separated by a time T (cf. Fig. 2.17).

Thus, the magnetization vector evolves analogously to the primary echo up to the second pulse, which rotates the magnetization fan about the x-axis. For $T \gg T_m$, the x-components of the rotated fan have vanished due to transverse relaxation. The third $\pi/2$-pulse rotates the remaining z-components of the magnetization vectors in the y-direction. The precession direction and frequency is the same as in the first evolution time τ. Hence, after a second time τ, an echo is formed with the magnetization vectors aligned on a circle centered along the y-axis.

The corresponding quantum-mechanical product operator calculation for a system of isolated spins is described by

$$\boldsymbol{\rho}_{eq} \xrightarrow{\pi/2\,\mathbf{S}_x} \xrightarrow{\tau\Omega_s\mathbf{S}_z} \xrightarrow{\pi/2\,\mathbf{S}_x} \xrightarrow{T\Omega_s\mathbf{S}_z} \xrightarrow{\pi/2\,\mathbf{S}_x} \xrightarrow{t\Omega_s\mathbf{S}_z} \boldsymbol{\rho}_6(\tau + T + t). \tag{2.95}$$

For $T \gg T_m$, $\boldsymbol{\rho}_6$ amounts to

$$\begin{aligned}\boldsymbol{\rho}_6(\tau + T + t) = &-\frac{1}{2}[\cos(\Omega_s(t-\tau)) + \cos(\Omega_s(t+\tau))]\mathbf{S}_y \\ &+\frac{1}{2}[\sin(\Omega_s(t-\tau)) + \sin(\Omega_s(t+\tau))]\mathbf{S}_x.\end{aligned} \tag{2.96}$$

The terms with arguments $\Omega_s(t-\tau)$ lead to an echo formation at $t = \tau$, the terms with $\Omega_s(t+\tau)$ form a so-called virtual echo at $t = -\tau$, but do not contribute to the stimulated echo. Hence, the stimulated echo is only half as intense as the primary Hahn echo.

In a different description, the sequence $\pi/2 - \tau - \pi/2$ creates a polarization grating (Fig. 2.20), which is stored for the time T. The last $\pi/2$-pulse induces a free induction decay of the grating, which shows the incidental shape of an echo.

2.10.1 3-Pulse ESEEM

In analogy to 2-pulse ESEEM, an envelope modulation of the stimulated echo is observed when the time delay T is incremented. For a two-spin system, the modulation part of the echo signal is given by

$$\begin{aligned}V_{3p}(\tau, T) = 1 - \frac{k}{4}\{&[1 - \cos(\omega_\beta\tau)][1 - \cos(\omega_\alpha(\tau + T))] \\ &+ [1 - \cos(\omega_\alpha\tau)]\big[1 - \cos(\omega_\beta(\tau + T))\big]\}.\end{aligned} \tag{2.97}$$

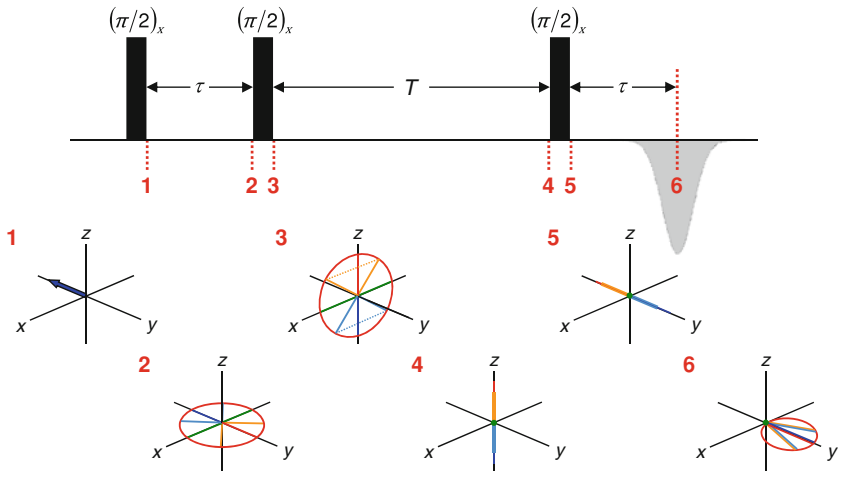

Fig. 2.17 ***Top*:** Formation of the stimulated echo after the pulse sequence $(\pi/2)_x - \tau - (\pi/2)_x - T - (\pi/2)_x - \tau$. *Bottom*: Graphical illustration of the magnetization vector (and selected vectors of the magnetization fan, respectively) at characteristic positions in the pulse sequence. Adapted from [79] with permission from the author

Unlike in 2-pulse ESEEM, no nuclear combination frequencies are observed. This significantly simplifies spectral interpretation. Further, an increased spectral resolution is achieved, since the echo decay is related to the phase memory time of the nuclear spins $T_m^{(n)}$, which is much longer than T_m. The experimental time trace of an electron coupled to a single nuclear spin is given by

$$V'_{3p}(\tau, T) = \exp\left(\frac{-\tau}{T_m^{(n)}}\right) V_{3p}(\tau, T). \tag{2.98}$$

Note that in contrast to 2-pulse ESEEM, modulations due to couplings with several nuclei are only multiplicative with respect to the electron spin manifold.

In Fig. 2.18, schematic nuclear frequency spectra are depicted in the framework of the two-spin system. In case of a negligible anisotropic hyperfine contribution, the modulation frequencies can be calculated by

$$\omega_\alpha = \left|\omega_I + \frac{A}{2}\right|, \omega_\beta = \left|\omega_I - \frac{A}{2}\right|. \tag{2.99}$$

Thus, a weak coupling case $|\omega_I| > |A/2|$ and a strong coupling case $|\omega_I| < |A/2|$ can be distinguished. In the weak coupling case, the peaks are symmetrically centered around ω_I and separated by A. In the strong coupling case, they are centered around $A/2$ and separated by $2\omega_I$.

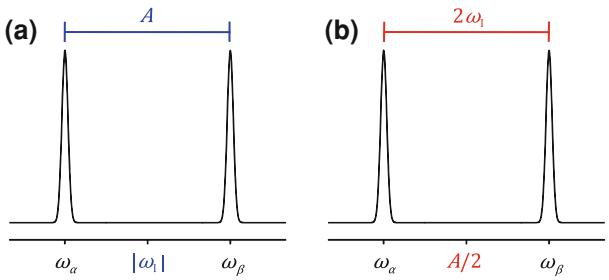

Fig. 2.18 Schematic nuclear frequency spectra for **a** weak coupling ($|\omega_I| > |A/2|$) and **b** strong coupling ($|\omega_I| < |A/2|$) in case of a negligible anisotropic hyperfine contribution. $\omega_I < 0$ and $A > 0$ are assumed, as observed for a proton with $g_n > 0$

2.10.2 Hyperfine Sublevel Correlation (HYSCORE) Spectroscopy

A modification of the 3-pulse ESEEM sequence is achieved by introduction of a non-selective π-pulse, which interchanges the nuclear coherences between the $|\alpha\rangle$ and $|\beta\rangle$ manifolds of the electron spin (Fig. 2.19a) [62]. The incrementation of both times prior to and after this pulse, t_1 and t_2, yields time-domain data in two dimensions which can be converted to 2D nuclear frequency spectra by Fourier transformation. This 2D EPR technique was invented in 1986 by Höfer et al. and named hyperfine sublevel correlation spectroscopy (HYSCORE).

Since spectral density is distributed over two dimensions, HYSCORE spectra provide for an improved resolution and contain information that cannot easily be retrieved by 1D ESEEM methods. The gain in spectral resolution is demonstrated in Fig. 2.19b, where HYSCORE spectra are schematically illustrated for the two-spin system in analogy to the 1D spectra in Fig. 2.18. Peaks of weakly coupled nuclei appear in the first quadrant, the second quadrant contains spectral information about strongly coupled nuclei.

2.10.3 Blind Spots

A feature of the 3-pulse ESEEM and the HYSCORE technique is a consequence of the factors $1 - \cos(\omega_{\alpha,\beta}\tau)$ in Eq. 2.97. For $\omega_{\beta,\alpha} = 2\pi n/\tau$ ($n \in \mathbb{N}_0$) the modulation at frequency $\omega_{\alpha,\beta}$ vanishes. This leads to so-called blind spots in the spectrum where the nuclear frequencies are efficiently suppressed.

The origin of the blindspots can also be described pictorially. The polarization grating created by a $\pi/2 - \tau - \pi/2$ pulse sequence is spaced by $1/\tau$, as illustrated in Fig. 2.20a. Nuclear modulations lead to a polarization transfer that changes the spectral shape and can be read out by the echo. However, if $\omega_{\beta,\alpha} = 2\pi n/\tau$,

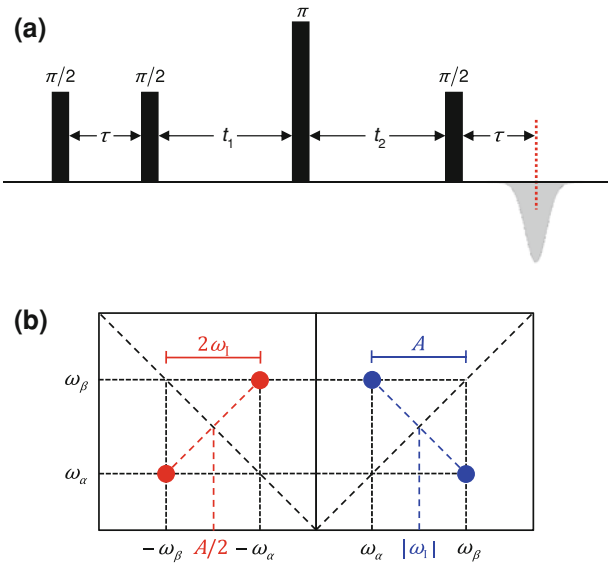

Fig. 2.19 **a** Pulse sequence for the hyperfine sublevel correlation (HYSCORE) experiment. **b** Schematic HYSCORE spectra. The spectral contribution of a weakly coupled nucleus manifests in the $(+,+)$ quadrant. Spectral features of a strongly coupled nucleus appear in the $(-,+)$ quadrant

a minimum is transferred to a minimum and a maximum is transferred to a maximum and the grating remains unaffected.

The distribution of blindspots in a HYSCORE spectrum with $\tau = 132$ ns is illustrated graphically in Fig. 2.20b. To assure the detection of all nuclear modulations, it is necessary to repeat experiments with different values of τ.

2.10.4 Phase Cycling

The $\pi/2 - \tau - \pi/2 - T - \pi/2$ pulse sequence does not only result in the formation of the stimulated echo, but also gives rise to unwanted echoes created by pairs of pulses (Fig. 2.21). The HYSCORE sequence generates even more unwanted echoes, which disturb the detected signal when evolution times are incremented.

These echoes can be efficiently suppressed by phase cycling. Here, one takes advantage of the fact that all echoes follow different coherence transfer pathways. With an appropriate phase cycle, only the pathway of the wanted echo is selected. Thus, the amplitude of this echo is maximized during the phase cycle, while all other echoes are annihilated.

A complete suppression of all echoes is achieved by a 4-step phase cycle for 3-pulse ESEEM and by a 16-step phase cycle for HYSCORE. However, since many coherence transfer paths do not lead to a refocusing, a 4-step phase

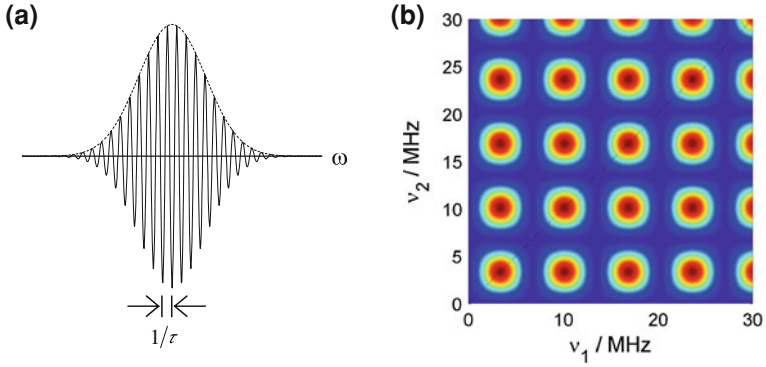

Fig. 2.20 **a** Polarization grating of a narrow EPR line created by a $\pi/2 - \tau - \pi/2$ pulse sequence. **b** Illustration of blind spots in the first quadrant of a HYSCORE spectrum for $\tau = 132$ ns assuming $|\omega_I| \gg |A/2|$. Spectral regions providing unsuppressed nuclear modulations are painted in warm colors while dark blue areas mark blindspots

cycle is usually sufficient [63]. In this thesis, an intermediate 8-step phase cycle was used.

2.11 Double Electron–Electron Resonance (DEER)

As introduced in Sects. 2.2.1 and 2.3.7, the characteristic dependence of dipole–dipole couplings can be utilized to retrieve distance distributions of two coupled electron spins. In the past, several pulse EPR methods were developed to separate the spin–spin interactions of electrons from other contributions of the spin Hamiltonian. Important single frequency techniques are the 2 + 1 method [64], SIFTER [65], and double quantum EPR [21, 66–68].

The application of two microwave frequencies (or two magnetic fields) allows for the spectral separation of a spin pair into an observer spin and a pump spin, which can be manipulated independently. In two-frequency methods, the separation of the spin–spin interactions is achieved by refocusing all interactions, including the spin–spin coupling by an echo sequence on the observer spin A. The spin–spin coupling is then reintroduced by a pump pulse on spin B that inverts the local magnetic field of spin A (Fig. 2.22c).

The selection of distinct observer and pump spins is also possible for a chemically identical spin pair. In this case, the anisotropy of the spectrum provides for the spectral separation. Typical observer and pump frequencies for nitroxides are shown in Fig. 2.22b. The frequency difference of $\sim$65 MHz allows for non-overlapping excitation profiles.

The original 3-pulse electron–electron double resonance (ELDOR) method consists of a primary echo subsequence on A [69, 70]. The pump pulse on B is

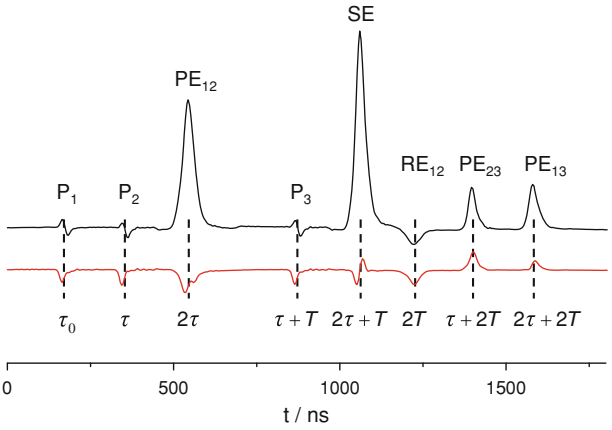

Fig. 2.21 Echoes generated by a $\pi/2-\tau-\pi/2-T-\pi/2$ pulse sequence applied to a 1:1 mixture of human serum albumin and 16-doxylstearic acid with $\tau = 180$ ns, $T = 600$ ns, and $t_P = 16$ ns. The real part is depicted in *black*, the imaginary part is given in *red*. The unwanted primary echoes (PE_{ij}) and the refocused echo, created by pairs of pulses (P_i,P_j), need to be annihilated by phase cyclings

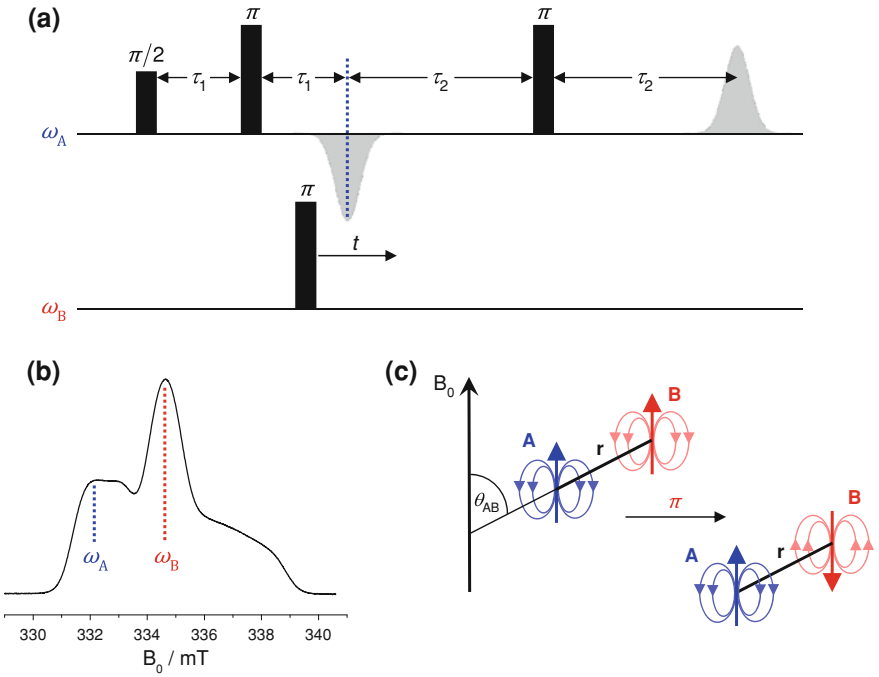

Fig. 2.22 **a** 4-Pulse sequence of the DEER experiment. **b** Typical nitroxide powder spectrum with spectral positions of the pump and observer frequencies. **c** Schematic illustration of the change of the local magnetic field caused by the pump π-pulse

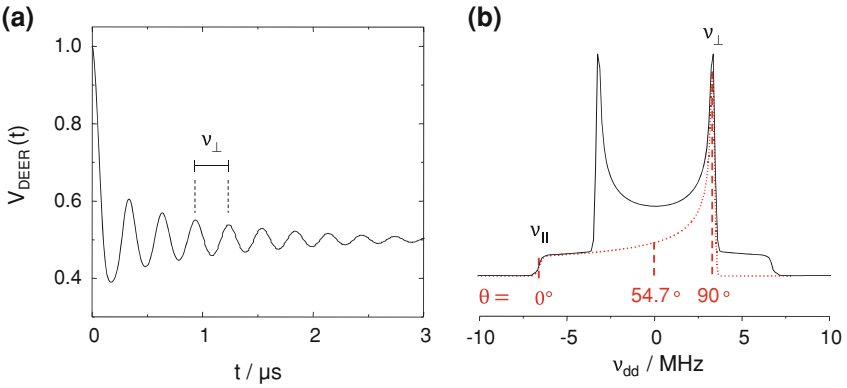

Fig. 2.23 **a** Calculated DEER time domain signal for two coupled nitroxides with $r = 2.5$ nm and $\sigma = 0.035$ nm and random orientational distribution in the matrix. **b** Corresponding Pake doublet in the frequency domain with characteristic frequency positions $\nu_\perp$ and $\nu_\parallel$ and specification of the angular contributions

implemented between the first and the second pulse. The data acquisition of the dipolar evolution is however limited by the deadtime after the first pulse. This problem can be overcome by introduction of a second refocusing pulse on A. The pulse sequence of this 4-pulse double electron–electron resonance (DEER) technique is shown in Fig. 2.22a [19, 71]. By variation of the time delay between the second pulse of the observer sequence and the pump pulse, a dipolar modulation of the refocused echo is observed, given by

$$V_{\mathrm{DEER}}(r,t) = 1 - \int_0^{\pi/2} \sin\theta_{\mathrm{AB}}\lambda(\theta_{\mathrm{AB}})[1 - \cos(\omega_{\mathrm{DD}}(\theta_{\mathrm{AB}})t)]d\theta_{\mathrm{AB}} \qquad (2.100)$$

with the dipolar frequency (cf. Eq. 2.42)

$$\omega_{\mathrm{DD}}(r,\theta_{\mathrm{AB}}) = \frac{\mu_0}{4\pi\hbar}\frac{g_{\mathrm{A}}g_{\mathrm{B}}\beta_{\mathrm{e}}^2}{r_{\mathrm{AB}}^3}(3\cos^2\theta_{\mathrm{AB}} - 1). \qquad (2.101)$$

θ_{AB} denotes the angle between the static magnetic field and the connection vector of the coupled electron spins, and λ is the orientation-dependent modulation depth parameter. For nitroxides at X-band, no pronounced orientation selection is observed at the observer and pump frequencies and λ is assumed orientation-independent. In this case, a Pake doublet is obtained by Fourier transformation of the time-domain data (Fig. 2.23).

The lowest retrievable distance is limited by the excitation bandwidth of the pump pulse, which has to equal the width of the dipolar Pake pattern. A 12 ns pump pulse provides for a lower limit of 1.5 nm. Note that no pulse sequence provides for the separation of dipole–dipole coupling and spin exchange coupling.

However, the latter contribution is usually negligible for distances exceeding 1.5 nm [22]. The upper limit of the accessible distance range is given by the maximum recordable dipolar evolution time and thus by τ_2. To unambiguously retrieve a distance, at least 5/8 of the modulation needs to be recorded. For model biradicals in rigid matrices, $\tau_2 = 6\,\mu s$ and $r_{max} = 8\,nm$ are accessible. For biological systems in water, $\tau_2 = 2.5\,\mu s$ and $r_{max} = 6\,nm$ are more realistic values.

In analogy to the ESEEM experiments, the modulation is superimposed by an exponentially decaying signal,

$$V_{DEER}^{hom}(t) = \exp\left(-\frac{2\pi\mu_0 g_1 g_2 \beta_n}{9\sqrt{3}\hbar}\lambda c_B t^{d/3}\right). \tag{2.102}$$

This background function originates from a superposition of dipolar couplings to homogeneously distributed electron spins with distances up to 40 nm. It is dependent on the concentration of excited B spins λc_B and the fractal dimension d of the sample. Hence, the experimental time trace amounts to

$$V'_{DEER}(t) = V_{DEER}^{hom}(t)\, V_{DEER}(t). \tag{2.103}$$

For a narrow distance distribution, the singularities of the Pake doublet $\nu_\perp$ can be easily identified and the corresponding distance can be directly calculated. However, it is a non-trivial problem to retrieve broad or complicated distance distributions $G(r)$ from the time (or frequency) domain data. In the framework of shell factorization analysis, the spherical volume around the observer spin is subdivided into thin shells. The probability of finding a spin B in a shell with thickness dr at distance r from the observer spin A is $4\pi r^2 dr G(r)$, where $G(r)$ is the wanted distance distribution. The normalized DEER signal (without orientation selection) is then given by

$$\ln\frac{V_{DEER}(t)}{V_{DEER}(0)} = -4\pi\lambda\int_{r_{min}}^{r_{max}} r^2 G(r)(1 - V_r(r,t))dr, \tag{2.104}$$

where $V_r(r,t)$ denotes the time domain signal within a certain thin shell.

One way to solve this equation is to simulate the dipolar modulations with a model distance distribution that is varied to fit the experimental time trace. Another way is to calculate the distance distribution directly from the time domain data. This mathematical problem is ill-posed, i.e. a slight distortion of the experimental signal may lead to strong distortions in the distance distribution. During the last years, several routes have been proposed to improve the reliability of the results with Tikhonov regularization being the current method of choice [72]. It is implemented in the comprehensive software package Deer Analysis2008 by Jeschke, which is used to analyze the DEER data in Sect. 3.2 [73]. This method is, however, not applicable if λ shows a pronounced orientation dependence. In this case, the first route has to be chosen and the dipolar modulations need to be simulated (cf. Sect. 3.4).

References

1. Gerlach W, Stern O (1921) Z Phys 8:110–111
2. Gerlach W, Stern O (1922) Z Phys 9:349–352
3. Gerlach W, Stern O (1922) Z Phys 9:353–355
4. Zeeman P (1897) Philos Mag 43:226
5. Zeeman P (1897) Nature 55:347
6. Uhlenbeck GE, Goudsmit S (1925) Naturwissenschaften 13:953–954
7. Uhlenbeck GE, Goudsmit S (1926) Nature 117:264–265
8. Zavoisky E (1945) J Phys USSR 9:211
9. Zavoisky E (1945) J Phys USSR 9:245
10. Purcell EM, Torrey HC, Pound RV (1946) Phys Rev 69:37–38
11. Bloch F, Hansen WW, Packard M (1946) Phys Rev 69:127
12. Ernst RR, Anderson WA (1966) Rev Sci Instrum 37:93–102
13. Blume RJ (1958) Phys Rev 109:1867–1873
14. Holczer K, Schmalbein D (1987) Bruker Rep 1:22
15. Höfer P, Maresch GG, Schmalbein D, Holczer K (1996) Bruker Rep 142:15
16. Likhtenshtein GI, Yamauchi J, Nakatsuji S, Smirnov AI, Tamura R (2008) Nitroxides—applications in chemistry, biomedicine and materials science. Wiley-VCH, Weinheim
17. Jeschke G (2006) Site-specific information on macromolecular materials by combining CW and pulsed ESR on spin probes. In: Schlick S (ed) Advanced ESR methods in polymer research. Wiley, New York
18. Hinderberger D, Jeschke G (2006) Site-specific characterization of structure and dynamics of complex materials by EPR spin probes. In: Webb GA (ed) Modern magnetic resonance. Springer, London
19. Jeschke G, Pannier M, Spiess HW (2000) Double electron–electron resonance. In: Berliner LJ, Eaton GR, Eaton SS (eds) Biological magnetic resonance, vol 19: distance measurements in biological systems by EPR. Kluwer Academic, New York
20. Jeschke G (2002) Chem Phys Chem 3:927–932
21. Borbat PP, Freed JH (2000) Double-quantum ESR and distance measurements. In: Berliner LJ, Eaton GR, Eaton SS (eds) Biological magnetic resonance, vol 19: distance measurements in biological systems by EPR. Kluwer Academic, New York
22. Jeschke G (2002) Macromol Rapid Commun 23:227–246
23. Schiemann O, Prisner TF (2007) Q Rev Biophys 40:1–53
24. Borbat PP, Costa-Filho AJ, Earle KA, Moscicki JK, Freed JH (2001) Science 291:266–269
25. Jeschke G, Polyhach Y (2007) Phys Chem Chem Phys 9:1895–1910
26. Schmidt-Rohr K, Spiess HW (1994) Multidimensional solid-state NMR and polymers. Academic Press, London
27. Dockter C, Volkov A, Bauer C, Polyhach Y, Joly-Lopez Z, Jeschke G, Paulsen H (2009) Proc Nat Acad Sci U S A 106:18485–18490
28. Hinderberger D, Spiess HW, Jeschke G (2010) Appl Magn Reson 37:657–683
29. Odom B, Hanneke D, D'Urso B, Gabrielse G (2006) Phys Rev Lett 97:030801
30. Bloch F (1946) Phys Rev 70:460–474
31. Abragam A, Pryce MHL (1951) Proc R Soc A: Math Phys Sci 205:135–153
32. Solomon EI, Hodgson KO (1998) Spectroscopic methods in bioinorganic chemistry. Clarendon, Oxford
33. McGarvey BR (1967) J Phys Chem 71:51–66
34. Molin YN, Salikhov KM, Zamaraev KI (1980) Spin exchange–principles and applications in chemistry and biology. Springer Verlag, Berlin
35. McConnell HM (1958) J Chem Phys 28:430–431
36. Hubbell WL, Cafiso DS, Altenbach C (2000) Nat Struct Biol 7:735–739
37. Kocherginsky N, Swartz HM (1995) Nitroxide spin labels - reactions in biology and chemistry. CRC Press, Boca Raton

38. Fajer PG, Brown L, Song L (2007) Practical pulsed dipolar ESR (DEER). In: Hemminga MA, Berliner LJ (eds) Biological magnetic resonance, vol 27: ESR spectroscopy in membrane biophysics. Springer, New York
39. D. Hinderberger (2004) Polyelectrolytes and their counterions studied by EPR spectroscopy, Doctoral Dissertation, Johannes Gutenberg-Universität, Mainz,
40. Beth AH, Robinson BH (1989) Nitrogen-15 and deuterium substituted spin labels for studies of very slow rotational motion. In: Berliner LJ, Reuben J (eds) Biological magnetic resonance, vol 8: Spin labeling—theory and applications. Plenum Press, New York
41. Edmonds AR (1960) Angular momentum in quantum mechanics. Princeton University Press, Princeton
42. Jeschke G, Schlick S (2006) Continuous-wave and pulsed ESR methods. In: Schlick S (ed) Advanced ESR methods in polymer research. Wiley, Hoboken
43. Kivelson D (1960) J Chem Phys 33:1094–1106
44. Freed JH, Fraenkel GK (1963) J Chem Phys 39:326–348
45. Schneider DJ, Freed JH (1989) Continuous-wave and pulsed ESR methods. In: Berliner LJ, Reuben J (eds) Biological magnetic resonance, vol 8: spin labeling–theory and applications. Plenum Press, New York
46. Meirovitch E, Freed JH (1984) J Phys Chem 88:4995–5004
47. Polimeno A, Freed JH (1995) J Phys Chem 99:10995–11006
48. Wegener C, Savitsky A, Pfeiffer M, Möbius K, Steinhoff HJ (2001) Appl Magn Reson 21:441–452
49. Bordignon E, Steinhoff HJ (2007) Membrane protein structure and dynamics studied by site-directed spin-labeling ESR. In: Hemminga MA, Berliner LJ (eds) Biological magnetic resonance, vol 27: ESR spectroscopy in membrane biophysics. Springer, New York
50. Stoll S, Schweiger A (2006) J Magn Reson 178:42–55
51. Stoll S, Schweiger A (2007) Easy spin: simulating cw ESR spectra. In: Hemminga MA, Berliner LJ (eds) Biological magnetic resonance, vol. 27: ESR spectroscopy in membrane biophysics. Springer, New York
52. Weil JA (1971) J Magn Reson 4:394–399
53. Goldman SA, Bruno GV, Polnaszek CF, Freed JH (1972) J Chem Phys 56:716–735
54. Hwang JS, Mason RP, Hwang LP, Freed JH (1975) J Phys Chem 79:489–511
55. Stoll S, Schweiger A (2003) Chem Phys Lett 380:464–470
56. Sørensen OW, Eich GW, Levitt MH, Bodenhausen G, Ernst RR (1983) Prog Nucl Magn Reson Spectrosc 16:163–192
57. Sørensen OW (1989) Prog Nucl Magn Reson Spectrosc 21:503–569
58. Hahn EL (1950) Phys Rev 80:580–594
59. Rowan LG, Hahn EL, Mims WB (1965) Phys Rev 137:A61–A71
60. Mims WB (1972) Phys Rev B 5:2409–2419
61. Mims WB, Davis JL, Peisach J (1990) J Magn Reson 86:273–292
62. Höfer P, Grupp A, Nebenführ H, Mehring M (1986) Chem Phys Lett 132:279–282
63. Gemperle C, Aebli G, Schweiger A, Ernst RR (1990) J Magn Reson 88:241–256
64. Kurshev VV, Raitsimring AM, Tsvetkov YD (1989) J Magn Reson 81:441–454
65. Jeschke G, Pannier M, Godt A, Spiess HW (2000) Chem Phys Lett 331:243–252
66. Saxena S, Freed JH (1996) Chem Phys Lett 251:102–110
67. Saxena S, Freed JH (1997) J Chem Phys 107:1317–1340
68. Borbat PP, Freed JH (1999) Chem Phys Lett 313:145–154
69. Milov AD, Salikhov KM, Shirov MD (1981) Fiz Tverd Tela 23:975–982
70. Milov AD, Maryasov AG, Tsvetkov YD (1998) Appl Magn Reson 15:107–143
71. Pannier M, Veit S, Godt A, Jeschke G, Spiess HW (2000) J Magn Reson 142:331–340
72. Jeschke G, Panek G, Godt A, Bender A, Paulsen H (2004) Appl Magn Reson 26:223–244
73. Jeschke G, Chechik V, Ionita P, Godt A, Zimmermann H, Banham J, Timmel CR, Hilger D, Jung H (2006) Appl Magn Reson 30:473–498

Bibliography

74. Atherton NM (1973) Principles of electron spin resonance. Ellis Horwood, Chichester
75. Weil A, Bolton JR, Wertz JE (1994) Electron paramagnetic resonance: elementary theory and practical applications. Wiley, New York
76. Schweiger A, Jeschke G (2001) Principles of pulse electron paramagnetic resonance. Oxford University Press, Oxford
77. Hore PJ, Jones JA, Wimperis S (2000) NMR: The toolkit. Oxford University Press, Oxford
78. Jeschke G (1998) Einführung in die ESR-Spektroskopie (lecture notes), Mainz
79. Jeschke G (2008) Kurze Einführung in die elektronenparamagnetische Resonanz-spektroskopie (lecture notes), Konstanz

http://www.springer.com/978-3-642-25134-4

Assessing the Functional Structure of Molecular Transporters by EPR Spectroscopy

J.N.Junk, M.

2012, XVI, 212 p., Hardcover
ISBN: 978-3-642-25134-4